9-2021

Analysis of Space to Ground Ladar Performance with Non-Traditional Optics

Prayant P.S. Hanjra

Analysis of Space-to-Ground LADAR Performance with Non-Traditional Optics

THESIS

Prayant P.S. Hanjra, 1st Lt, USAF

AFIT-ENP-MS-21-S-030

DEPARTMENT OF THE AIR FORCE
AIR UNIVERSITY

AIR FORCE INSTITUTE OF TECHNOLOGY

Wright-Patterson Air Force Base, Ohio

AFIT-ENP-MS-21-S-030

ANALYSIS OF SPACE TO GROUND LADAR PERFORMANCE WITH NON-TRADITIONAL OPTICS

THESIS

Presented to the Faculty

Department of Engineering Physics

Graduate School of Engineering and Management

Air Force Institute of Technology

Air University

Air Education and Training Command

in Partial Fulfillment of the Requirements for the

Degree of Master of Science in Optical Sciences & Engineering

Prayant P.S. Hanjra, B.S. Physics

1st Lt, USAF

June 21, 2021

AFIT-ENP-MS-21-S-030

ANALYSIS OF SPACE TO GROUND LADAR PERFORMANCE WITH NON-TRADITIONAL OPTICS

THESIS

Prayant P.S. Hanjra, B.S. Physics
1st Lt, USAF

Committee Membership:

Dr. Steven Fiorino
Chair

Dr. Jack McCrae
Member

Dr. David Rabb
Member

Dr. Andre Van Rynbach
Member

Abstract

Two major obstacles to space-based LADAR systems are low power returns from targets and size and weight limitations on transporting large optics into orbit. Signals incur significant losses during roundtrip propagation through the atmosphere and diffuse scattering off of targets. The effects of atmospheric losses are simulated with the Laser Environmental Effects Definition and Reference (LEEDR) simulator and High Energy Laser End to End Operational Simulation (HELEEOS) for a variety of atmospheric and environmental conditions across the globe. These losses are used to determine if sufficient power would reach a space-borne receiver. Optics in space tend to be large in order to aid in capturing sufficient power. However, these optics quickly become prohibitively large and heavy to transport in a satellite. Many non-traditional optics have emerged in recent years that show promise for providing lightweight and volume constrained solutions. One such example is printed, gradient index (GRIN) optics. These optics were acquired and characterized for their potential use in creating LADAR systems in space. The results from these characterizations were used to create more robust photon link budgets and simulations. The feasibility of space based LADAR is reported from a radiometric standpoint. This study uses modeling to predict signal-to-noise ratios for diverse environments, partially validates the models with ground-truth tests, and evaluates the utility of novel non-traditional optics.

For my parents: my successes are the fruits of your labor.

Acknowledgements

I would like to give thanks to some of the many people who helped me in my endeavors.

First, thank you Dr. Fiorino for your endless patience, encouragement, and enthusiasm. Whenever I was feeling overwhelmed or at a dead end, our meetings would always help ease my worries. Thank you for always finding more opportunities for me.

Andre, thank you for being an incredible friend and mentor. Your steadfast belief in me and willingness to explain (oftentimes re-explain) concepts always helped me take on greater and greater tasks. I have relished working with and learning from you these past few years.

To the good people of the AFRL/RYMM − the Sensors Directorate's Active Electro-Optical Sensing branch − thank you for welcoming me and giving me an environment that encouraged curiosity, risk-taking, and growth.

Lastly, and most importantly, thank you to my family for never doubting me and always keeping me grounded.

Prayant P.S. Hanjra

Table of Contents

Page

List of Figures

List of Tables

ANALYSIS OF SPACE TO GROUND LADAR PERFORMANCE WITH NON-TRADITIONAL OPTICS

I. Introduction

1.1 Motivation

Laser Detection and Ranging, commonly known as LADAR, is a method of remote sensing in which light of visible or infrared wavelengths is cast onto targets and information is extracted from the reflections. The reflections can be measured through several modalities. The simplest is direct detection in which the returns are time stamped upon arrival at at a detector. The time is then divided by the speed of light to find the roundtrip distance the pulse of light traveled. This data can be used to develop a three-dimensional (3D) map of a target scene and extract information on how the target varies with depth. Since it is an active electro-optical system, it can be conducted in both daytime and nighttime conditions, as opposed to passive imagers like many visible wavelength cameras.

Direct detect LADAR systems have found use in many land and aerial based platforms. Due to their ability to render 3D maps of targets and distinguish depth, airborne direct detect systems have been used in mapping heavily forested areas to see below canopies [1]. The same concept has been used over lakes to track sea life and lakebeds [2]. These systems are also used in land surveying and urban mapping. Some low resolution direct detect systems have been placed in Earth's orbit by NASA for elevation mapping of arctic regions, but these systems do not have the capability to create images in two-dimensions [3].

Placing a LADAR detector capable of imaging in two-dimensions in Earth's orbit could allow for vast improvements on existing intelligence, surveillance, and reconnaissance (ISR) capabilities that are currently in orbit. Traditional ISR satellites are limited in their hours of operability and/or resolution.

Operability limitations come from the Earth's rotation. Passive sensors, those which do not illuminate their targets but depend on lighting from the Sun, are only usable for the hours that their intended targets are experiencing daytime. Active sensors have their own light sources with which to illuminate their targets and can bypass this operability issue.

Resolution limitations are a consequence of the wavelength of the light source. Resolution is directly proportional to the wavelength of the light being captured [4]. Smaller wavelengths thereby imply smaller distances that can be resolved, which amounts to greater detail in images.

Current active sensors operate in the radio frequency (RF) band of the electromagnetic spectrum. The RF band has much longer wavelengths (centimeters to meters) than that of the visible or infrared (IR) light which comes from the Sun (nanometers to microns). So while these active sensors overcome the operability limitations of passive sensors, they are limited in resolution due to their long wavelengths. A LADAR system that would operate in the short wave infrared (SWIR) band would retain RF sensors' ability to sense under low lighting conditions while improving resolution by moving to shorter wavelengths.

One major drawback, however, is that SWIR wavelengths are much more susceptible to scattering and absorption in the Earth's atmosphere than RF wavelengths. Space based LADAR can only provide the aforementioned advantages if it can overcome the attenuation due to Earth's atmosphere. Thus, in order to realize the feasibility of a space based LADAR sensor, SWIR attenuation through the atmosphere

requires further study.

In addition to signal loss, other limiting factors in space sensing are size and weight. Satellites are inherently volume constrained. Additionally, they are weight constrained due to limited fuel supplies. Essentially, larger, heavier payloads are harder to transport to orbit. In recent years, novel optical components have emerged that can circumvent these obstacles.

Light-weight polymers have begun to appear in lenses. These provide the advantage of weight reduction over conventional glass lenses which are far denser and heavier. Flat, gradient index (GRIN) lenses are one type that provide the weight advantages while also reducing volume. Whereas a large, glass lens takes up considerable space due to its spherical surface, a GRIN lens can accomplish the same focusing effect while being completely flat – only millimeters in depth. GRIN lenses may provide a viable path forward for space based LADAR by leveraging their weight and volume savings. Therefore, they require further study as well.

1.2 Objective

Understanding laser transmission through the atmosphere informs several areas of research including free space optical communications, laser weaponry, and ISR. The Laser Environmental Effects Definition and Reference (LEEDR) is a model that characterizes atmospheric effects on radiation propagation. LEEDR contains a database of historical, worldwide, weather data and computes laser transmission via numerical weather predictions. LEEDR informs the High Energy Laser End-to-End Operational Simulation (HELEEOS) which estimates beam shape and intensity for a laser propagated through the atmosphere. Coupled together, these models provide the ability to estimate signal losses for a space based LADAR at any point on the globe under any weather conditions. Accordingly, the research herein uses LEEDR and HELEEOS

simulations to identify an atmospheric transmission threshold required to generate LADAR imagery.

The simulations themselves are validated with ground-based, laser transmission measurements. Ultimately, the simulations can accurately predict laser transmission with only a few inputs: pressure, temperature, humidity (PTH), and particle count. This testing lends credence to the models and enables their use in predicting LADAR performance at large distances.

While the models aid in understanding laser transmission through the atmosphere, the atmosphere is not the only potential area of signal loss. The optical components themselves can attenuate signal by absorbing or scattering light. In order to conduct a robust study of laser transmission for a space based LADAR, the GRIN lenses' transmission efficiency and focusing qualities are tested as well.

Ultimately, the three primary objectives of this study are as follows: validating the LEEDR and HELEEOS models in order to bolster their predictions, establishing a threshold atmospheric transmission needed for space-based LADAR and quantifying its probability of occurrence, and appraising the performance of GRIN lenses in the context of a space-based LADAR sensor.

1.3 Organizational Structure

This document begins with a Chapter II background of theory and concepts that are necessary to understand the research herein. Chapter III describes in detail the experimental methods for validating the models, executing the models, and characterizing the non-traditional optics. Chapter IV holds the results of the experiments and analyzes their meaning in the context of this thesis. Lastly, Chapter V provides a summary and potential future research efforts.

II. Background

The purpose of this chapter is to summarize the necessary concepts and theories that are used in the following research. The first section provides a background on the basics of optics. Then, LADAR systems are discussed in their principles of operation, methods of detection, and history. Light propagation through the atmosphere and methods of simulating its effects are discussed. Finally, a summary of gradient index optics is presented.

2.1 Optics Background

Laser Detection and Ranging (LADAR) is a means of remote sensing through lasing targets and measuring the returns. LADAR is predicated on the fundamental wave-particle nature of light. Thus, in order to fully grasp LADAR, an understanding of the foundations of light propagation is required.

Light exhibits both wavelike and particle-like properties. Both of these can be examined individually or in conjunction to study light. In 1905, Albert Einstein proposed that light, and the energy it carries, is quantized [4]. That is, it exists in discrete packages rather than a continuum. These packets of light became known as photons. Photons are the massless, particle-like manifestation of light. The energy of a photon is quantized according to the wavelength (or frequency) the light wave it is exhibiting. This energy is found by:

$$E = \frac{hc}{\lambda} = h\nu \tag{1}$$

where h is Planck's constant, c is the speed of light, λ is the wavelength of the light, and ν is the frequency of the light [4].

Although light consists of these discrete packets of energy, it also exhibits wavelike

properties. This is a consequence of quantum mechanics and is also observed with subatomic particles such as electrons. This phenomenon is known as the wave-particle duality. Since light behaves as a wave, the electromagnetic field of monochromatic light can be represented by a harmonic function in time [5]:

$$u(r,t) = a(r)\cos(2\pi\nu rt + \phi(r)) \tag{2}$$

Where r represents a position vector, $a(r)$ is the amplitude of the field, ν is the frequency, t is time, and ϕ is the phase. Whereas $u(r,t)$ is only the real part of the light field, the field can be more completely represented in complex form [5]:

$$U(r,t) = a(r)e^{i2\pi\nu t}e^{i\phi(r)} \tag{3}$$

The frequency of light, ν, is extremely high at optical (visible) wavelengths – on the order of THz. This is much faster than any detector can operate. So detectors, such as the human eye, average the light over comparatively long periods and observe its intensity. Intensity, I, is the average power per area of a light field (Watts/cm^2) and is found by taking squared magnitude of the field.

$$I = |U(r,t)^2| = U(r,t) \times U(r,t)^* \tag{4}$$

The complex representation is more complete because it allows for an easy understanding of the interaction between waves. When two fields overlap, they can constructively or destructively interfere with one another. This was famously demonstrated in Thomas Young's Double Slit experiment in which a point source of light was passed through two slits [4]. This resulted in an interference pattern of bright and dark fringes on a distant screen. The interference pattern is the result of phase differences in the light fields. To see this clearly, take the case of two fields of light

that are identical in frequency and differ only in phase:

$$\begin{aligned}
|U_1 + U_2|^2 &= |U_1 e^{i(2\pi\nu t + \phi_1(r))} + U_2 e^{i(2\pi\nu t + \phi_2(r))}|^2 \\
&= U_1^2 + U_2^2 + U_1 U_2 e^{(\phi_1(r) - \phi_2(r))} + U_1 U_2 e^{(\phi_2(r) - \phi_1(r))} \\
&= U_1^2 + U_2^2 + 2U_1 U_2 \cos(\phi_1(r) - \phi_2(r)) \\
&= I_1 + I_2 + 2\sqrt{I_1 I_2}\cos(\phi_1(r) - \phi_2(r)) \qquad (5)
\end{aligned}$$

The resulting fringe pattern is cosinusoidal with position. If waves converging on a point are completely in phase, that is, $\phi_1 - \phi_2 = 0$, the resulting intensity is four times the individual intensity – a bright spot. Conversely, when they are completely out of phase, that is $\phi_1 - \phi_2 = \pi$, the two fields destructively interfere with each other and result in zero intensity – a dark spot.

So, while detectors can only directly record the intensity of light, the intensity pattern itself can reveal information about the phase. This provides a way to measure the rapidly oscillating light field which is otherwise unobservable. This is a consequence of the wave nature of light.

While interference can be useful for discerning phase information, it also imposes limitations on imaging capabilities. This can be seen if Young's Double Slit experiment is simplified to consider light projection through a single aperture. If light exhibited only particle-like properties, one would expect light to appear directly behind the aperture and cast a perfect shadow elsewhere. However, this is not the case. The pattern on the screen is spread out and encompasses a region larger than the aperture itself. This is due to diffraction – the spreading of waves as they pass through an aperture or around the edges of an obstacle [6]. The spreading causes the light to interfere with itself and create interference patterns known as diffraction patterns. This phenomenon imposes a fundamental limit on how narrowly light can

stay collimated, or how finely it can be brought to focus by a lens. This limit is known as the diffraction limit.

For the case of a circular aperture, the resulting diffraction pattern, also known as the point spread function (PSF), is a series of concentric rings around a central bright lobe, known as an Airy disk. If the images of two objects imaged through the same aperture are to be differentiated, or resolved, they must be separated such that the central maximum of one image overlaps with the first minimum of the second image. This is known as the Rayleigh criterion and is defined as follows [4]:

$$\theta = 1.22\frac{\lambda}{D} \tag{6}$$

Where θ is the half angle separation of the objects as measured from the point of observation, λ is the wavelength of light, and D is the diameter of the diffracting aperture. This is known as the cross-range resolution due to the fact that it is the aperture's ability to resolve details across its field of view. This is separate from range resolution for 3D imaging, which is discussed in the following section. The Rayleigh criterion can be seen along with the Airy pattern in one dimension in Fig. 1.

An even better method of determining the resolving capability of a system than the Rayleigh criterion, which is somewhat arbitrary, is to examine the Modulation Transfer Function (MTF) [4, 7]. The modulation in an image is a measure of the maximum contrast that can be seen in an image. That is, the ratio of the contrast between the brightest and dimmest parts of an image to the average brightness of the whole image.

$$Modulation = \frac{I_{max} - I_{min}}{I_{max} + I_{min}} \tag{7}$$

Due to the finite sizes of lenses, not all rays of light emanating from an object will reach and be imaged by a lens. Because of this, there is a loss of information. More

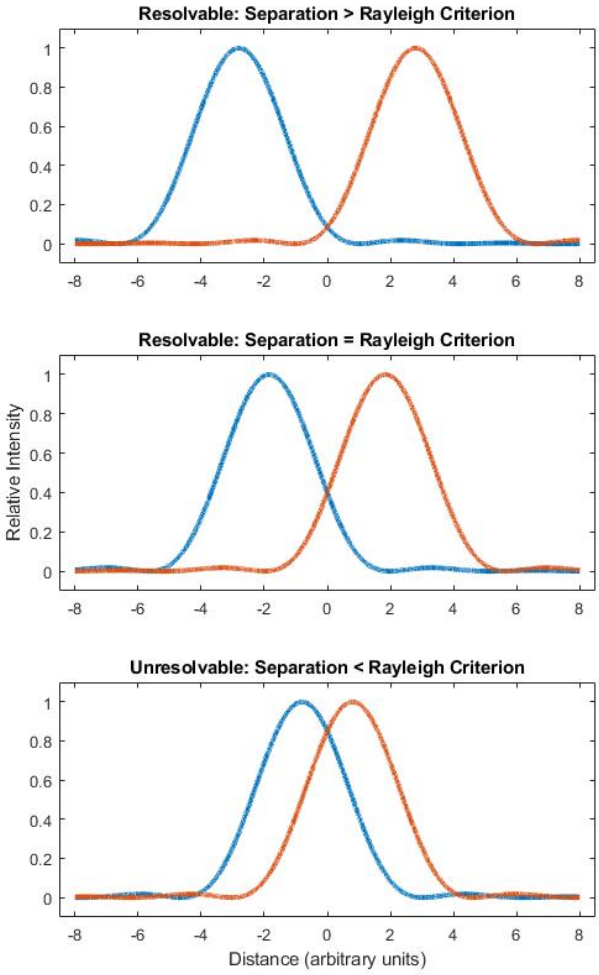

Figure 1. Airy patterns in one-dimension as seen approaching and passing the Rayleigh criterion for resolution, going from resolved to unresolved.

specifically, sharp edges on objects, which are indicative of high spatial frequency, will not appear as sharply in images as demonstrated by Fig. 2. For objects that are spaced closely together and have high spatial frequency, this blurring can wash out an image entirely and make the object entirely unresolvable. This imposes a fundamental cutoff spatial frequency that can be resolved. For a circular aperture,

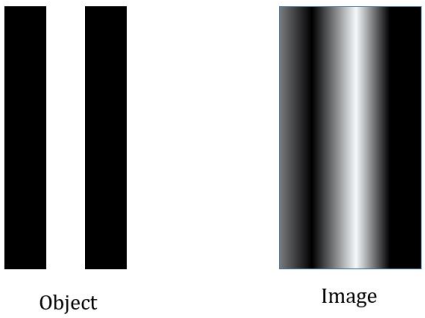

Figure 2. The modulation in contrast of sharp edges caused by lens' finite aperture.

this cutoff frequency is given by [5]:

$$f_c = \frac{1}{2\lambda F\#} \tag{8}$$

where $F\#$ is defined as the ratio of the focal length to the diameter of a lens.

This relationship between a system's physical dimensions and the spatial frequencies it sees is more formally understood by looking at the Optical Transfer Function (OTF). Since position and frequency are related by a Fourier Transform, the OTF is defined as the Fourier Transform of the PSF [8]. The PSF contains the spatial information of the image plane. Fourier Transforming the PSF yields the spatial frequency information of the image plane.

For a diffraction limited, circular aperture, the OTF is given by the Fourier Transform of the Airy disk [8]:

$$H(f) = \frac{2}{\pi}\left[\arccos\left(\frac{f}{2f_c}\right) - \frac{f}{2f_c}\sqrt{\left(1-\left(\frac{f}{2f_c}\right)^2\right)}\right]; f \leq 2f_c \tag{9}$$

where f represents spatial frequency in the radial direction and f_c is the cutoff frequency.

The MTF is simply the modulus of the OTF, that is, $|H(f)|$. The MTF of a

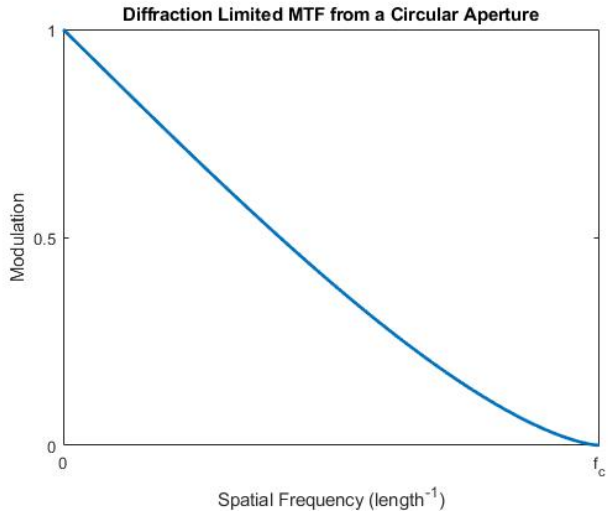

Figure 3. The diffraction limited MTF of a circular aperture, the ideal case.

diffraction limited circular aperture is shown graphically in Fig. 3. The OTF and MTF are identical in this case because the OTF is positive for $0 \leq f \leq f_c$.

To understand what the OTF and MTF will look like for an aberrated aperture, it is useful to examine the case of a square aperture as shown in Fig. 4. The OTF for a square aperture with focusing error aberration is as follows:

$$H(f_x, f_y) = \Lambda\left(\frac{f_x}{2f_c}\right)\Lambda\left(\frac{f_y}{2f_c}\right) \times \left[\frac{8W_m}{\lambda}\left(\frac{f_x}{2f_c}\right)\left(1 - \frac{|f_x|}{2f_c}\right)\right]\left[\frac{8W_m}{\lambda}\left(\frac{f_y}{2f_c}\right)\left(1 - \frac{|f_y|}{2f_c}\right)\right] \tag{10}$$

where f_x and f_y represent spatial frequencies in the x- and y-directions, $\Lambda(x)$ is the triangle function $1 - |x|$, and W_m is the width of the square. The shapes of the curves and the points at which the modulation drops to zero give indications of how much aberration a lens exhibits.

The wavelike nature of light is responsible much of what has been discussed thus far: diffraction and the MTF. Diffraction, in turn, is responsible for light divergence. Diffraction is not often noticeable in natural lighting. This is due to the wide spectrum

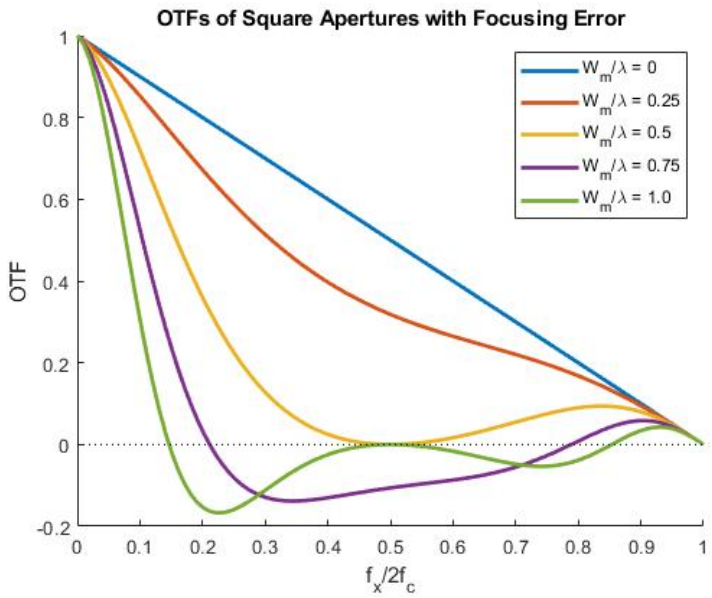

Figure 4. The OTF for a square aperture with the ideal case ($\mathbf{W}_m/\lambda = 0$) shown and aberrated cases ($\mathbf{W}_m/\lambda > 0$) shown. The aberration shown here is focusing error. The negative portions of the OTF indicate a phase reversal.

of light seen from the Sun or common indoor lighting. Any interference patterns that would be observed are averaged out by the wide range of wavelengths and wavefronts simultaneously constructively and destructively interfering with each other. In other words, the light is incoherent. However, for systems that rely on coherent, monochromatic or near monochromatic light, such as that from lasers, the effects of diffraction and beam divergence become more pronounced and require close attention. A laser can produce well collimated light but, inevitably, the light will begin to diverge as it propagates.

A beam's divergence is inversely proportional to its minimum spot size. The radius of the minimum spot size is referred to as the beam waist. The waist is defined to be the radial point at which the field's amplitude falls to $1/e$ of its maximum, or, identically, when the intensity falls to $1/e^2$. For a Gaussian beam, the beam width

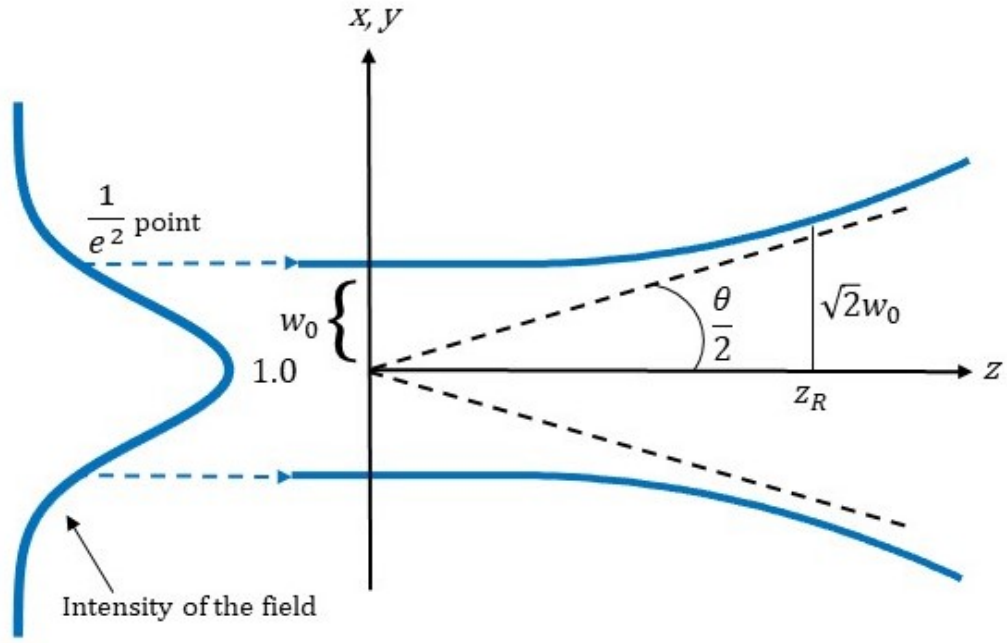

Figure 5. Divergence of a Gaussian beam. The beam waist is the smallest radius at the center, defined as the $1/e^2$ point for intensity. After the beam reaches the Rayleigh length at $\sqrt{2}w_0$ the beam begins to diverge linearly. Adapted from [9].

follows a hyperbolic profile and is governed by the following equation:

$$w^2(z) = w_0^2 \left[1 + \left(\frac{\lambda_0 z}{\pi n w_0^2}\right)^2\right] \tag{11}$$

where w_0 is the beam waist, λ_0 is the wavelength of interest, n is the index of refraction of the propagating medium, and z is distance along the optical axis [9]. The location of the waist along the z-axis is commonly made the zero point. This equation is often simplified with the definition and substitution of the Rayleigh range:

$$z_R = \frac{\pi n w_0^2}{\lambda_0} \tag{12}$$

The Rayleigh range is the point along the z-axis at which the beam begins to diverge linearly. This occurs when the beam width is $\sqrt{2}w_0$. This can be seem pictorally in

Fig. 5. For large propagation lengths that extend well beyond the Rayleigh range, Equation 11 simplifies to:

$$w(z >> z_R) = \frac{w_0 z}{z_R} = \frac{\lambda_0 z}{\pi n w_0} \tag{13}$$

From this equation it is clear to see that a beam with a larger waist will diverge less. This is a desirable characteristic for systems that require beams to stay collimated over long paths.

Laser detection and ranging is predicated on laser illumination and therefore applies the aforementioned concepts.

2.2 LADAR

Laser Detection and Ranging, LADAR, is a method of remote sensing by means of measuring light reflections from targets. The terms LiDAR (Light Detection and Ranging) and Laser Radar are used interchangeably and refer to the same concept. The term LADAR will be used moving forward.

The earliest form of LADAR was range finding which is considered direct detection laser ranging [10]. This modality of LADAR measures a laser pulse's roundtrip time of flight to determine distance to targets. It relies solely on the particle nature of light – the photon – so it does not record any phase information. In direct detection, a pulse of light is sent out and triggers the camera's internal clock to start. The light then reflects off a target and travels back to the camera. Once the light is detected by the camera, the clock stops. This time is recorded as the roundtrip time-of-flight (TOF) for the pulse of light. The TOF is then used to calculate the distance, or range, from the system to the target. For the case of a collocated laser and camera,

the distance from the system to the target is easily calculated by:

$$D = \frac{ct}{2} \tag{14}$$

where c is the speed of light and t is the roundtrip TOF.

This is known as a monostatic system since the light is both transmitted and received through the same optic. When the laser and camera are separated and the light is received through a different optic, the system is considered to be bistatic. This can be seen in Fig. 6. Depending on the separation, range calculations for bistatic systems can become more complex as they must take into account the spatial separation of the laser and camera and adjust clock timing accordingly.

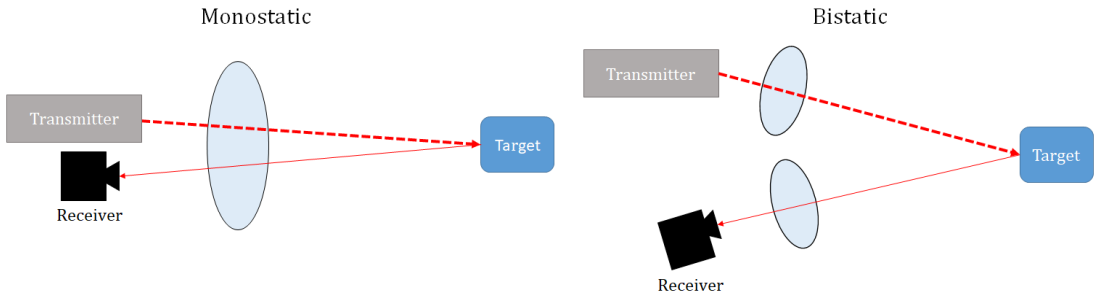

Figure 6. Diagram of monostatic vs. bistatic LADAR. In a monostatic configuration, as seen on the left, the transmit and receive components share the same optics. In a bistatic configuration, as seen on the right, they have separate optics.

The raw data from a direct detection system is a collection of times that must be sorted in order to discern useful range data. The raw data set will consist of information on all targets in the scene that reflected the laser pulse. This includes objects that are obscured from sight but still receive illumination. An analogy is to consider the varying depths in a rainforest. While from an aerial view only the dense canopy is visible, light is still reaching through to the ground level. This then implies that light from the ground level might also be reflected back out through the canopy.

Though this light is not processed by the naked eye, a direct detect system captures it. To differentiate between points at different depths, these systems group sections of the scene by their range values, a process known as range-gating. Within each range gate there will be peaks in photon count at various times indicating different target depths [11] (see Fig. 7). Identifying these peaks can help discern objects that appear to be at the same depth but are in reality separated. An example separating ambiguous targets based on peak returns is shown in Figs. 8a and 8b.

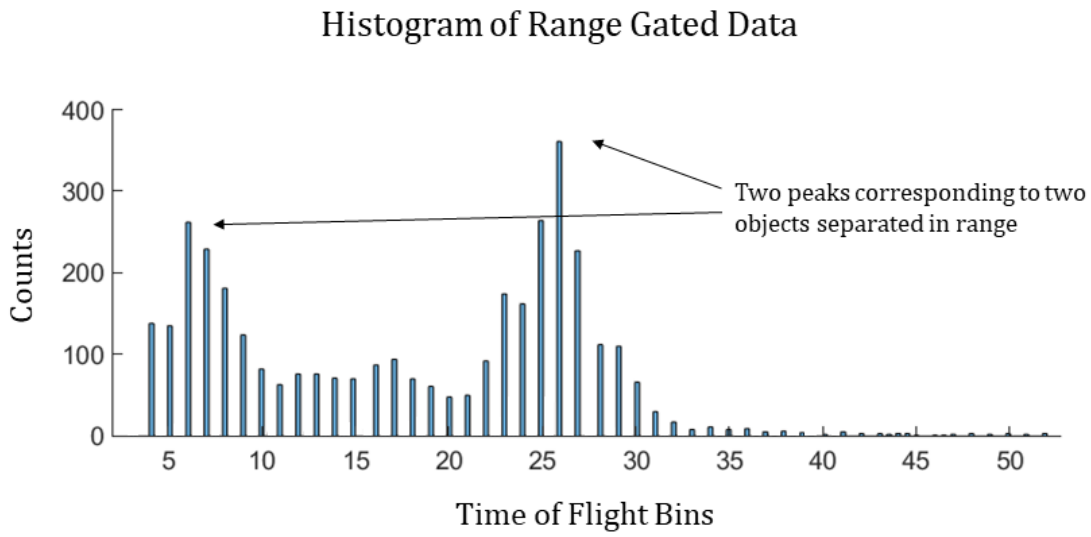

Figure 7. Histogram of range gated data. This is time time-of-flight data from one pixel. Each bin represents increments of 0.5ns. The counts signify how many times a photon was detected at that particular bin over the course of the integration time. This data was taken in the laboratory as part of this thesis research.

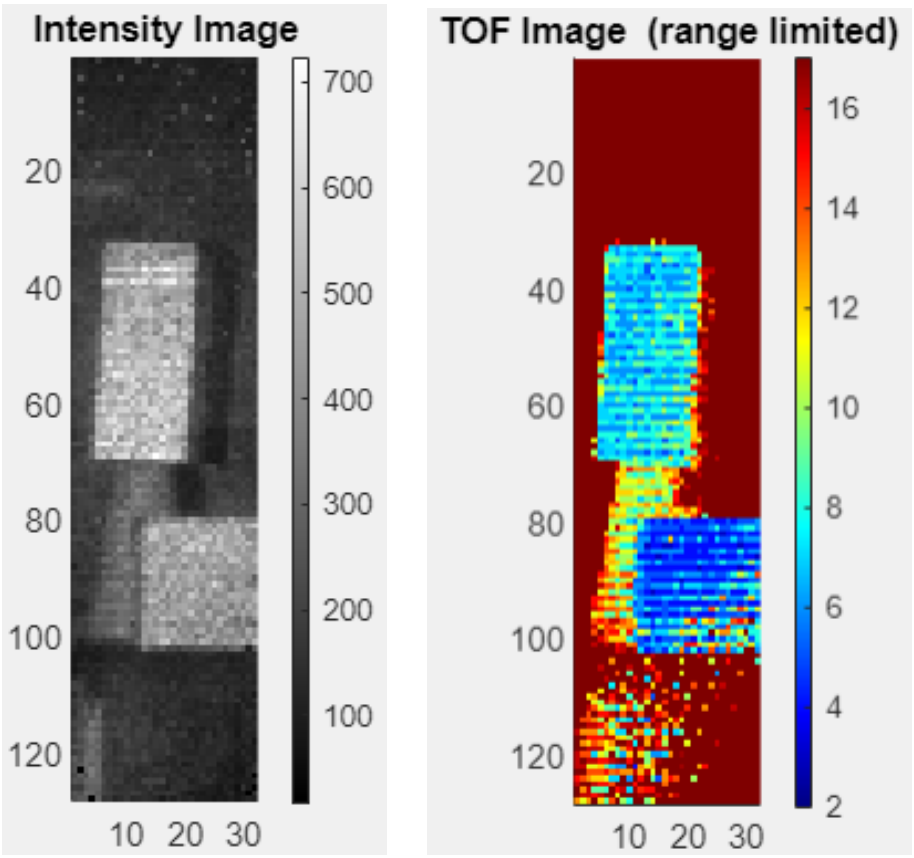

(a) An intensity image of two cardboard boxes separated in depth. The color scale indicates the pixel value.

(b) A range gated image of two cardboard boxes separated in depth. The boxes are seen clearly in two different shades of blue. The lighter blue indicates a deeper depth. The multi-colored pixels towards the bottom left are noise returns. The color scale indicates range bin where each range bin is 0.25 nanosecond wide.

Figure 8. Intensity and range gated images of two cardboard boxes separated in depth. The boxes are difficult to differentiate in depth using only the intensity image on the left. When range-gating is enabled on the right, it is easy to distinguish how far one box is from the other. Here, the boxes are separated by about three feet. This data was taken in the laboratory as part of this thesis research.

A user can look at different depths in a scene and see what lies at each layer. By viewing the data in this way, a user can look past obscurants such as tree tops over a rainforest, a process known as foliage penetration (FOPEN). Researchers at MIT's Lincoln Laboratory, in conjunction with the Defense Advanced Research Projects Agency (DARPA), have created several such LADAR systems, such as JIGSAW, and used them in airborne settings [12]. JIGSAW was a low altitude FOPEN capable

LADAR which operated in the visible spectrum (532nm) and was capable of real-time 3D imaging [13]. It is important to note that microwave radar also has the capability of FOPEN but at much lower resolution quality due to the long wavelengths (see Equation 6) [12].

The degree to which a system can discern ranges, its range resolution, can be limited by the length of the laser pulse. Considering that light travels at approximately 0.3 meter per nanosecond, a pulse lasting 10ns will then spread out over a distance of 3 meters. Since the pulse travels the distance between the target and system twice for a roundtrip, this means that returns from the pulse will represent a region of 1.5 meters. A target in the scene will reflect during the whole duration of the pulse, meaning the target will be associated with multiple time stamps. This is a problem because only one can represent the true distance. The pulse length, therefore, is directly related to range resolution by introducing ambiguity in the range profile of a target. So, a shorter pulse corresponds to a shorter resolvable depth. Only if the pulse were a perfect delta function would the time of flight unambiguously represent the true distance and the system would have perfect range resolution. From Equation 14, the resolution in that case would approach zero [14].

The timing resolution of the camera also impacts the range resolution. Geiger mode avalanche photodiodes (GmAPDs), are single photon sensitive, time of flight cameras that bin photons together according to time intervals. They do not record the exact time of arrival. Instead, they create range gates comprised of many time intervals and wait for a photon to arrive. Then, through data processing, the photon detections can be organized into bins according to which time interval they arrived in. This binning can be viewed as a histogram of TOFs as seen in Fig. 7. The length of the gate and the number of bins it has determine the level of detail that can be distinguished. For example, a range gate of 30ns comprised of 10 bins means that

the camera will be able to distinguish photons only if their arrival time is greater than 3ns apart. This corresponds to a range resolution of 1/2 meter accounting for the roundtrip of the photon. If targets are separated by less than 1/2 meter, the returns from those targets will be randomly split between two bins and become indistinguishable. With adequate range resolution, users can distinguish different range strata within images and analyze them independently from the whole image.

Kutteruf et. al. found that when two targets were clearly separated with nothing obscuring a GmAPD camera's line of sight, the camera timing resolution was the limiting factor [14]. That is, with a 0.25ns bin size, they were able to successfully distinguish objects 1.5 inches apart. When there was an obscurant, a mesh basket, the objects were too closely spaced to distinguish with one pulse. Ordinarily, even with an obscurant, a LADAR system will detect reflections from the target in the background as a small peak in the TOF histogram. The returns from the foreground can be filtered out to reveal the obscured object. However, in this study, not enough returns were detected to distinguish the two peaks. Laser power or the camera's integration time (range gate) can be increased to compensate, but this shows that the limiting factor was the laser pulse since the two objects were blended together in the ambiguity caused by the pulse length. The limiting factor in depth resolution can variably be the pulse length or camera's timing resolution depending on the scenario.

Researchers have taken this concept of distinguishing ranges in two dimensional images and have found myriad applications. Archaeologists have employed airborne LADARs to see beneath canopies in Mesoamerica by filtering out returns that correspond to the canopy height. Through this process, they have revealed hundreds of previously undiscovered sites, many of which are inaccessible by foot [1]. LADAR has also been used to see beneath water surfaces and aid in underwater mapping – bathymetry. Airborne Lidar Bathymetry (ALB) is a means of employing direct de-

tection LADAR to map water depths in rivers and lakes. Researchers have been able to measure water depths from 1.5m to 60m using this method and track the presence of invasive fish species [2, 15].

In order to perform this sort of range delineation, a sensor must receive enough photons from the target scene. The fundamental tool in predicting whether or not a LADAR system will receive a sufficient signal is the LADAR range equation. There are many variants of the equation, each taking into account slightly different variables, but all of which have the ultimate intent of predicting the amount of signal a detector will receive. Below is one example adapted from [10] for a Lambertian, or diffuse, target that is normal to the line of sight. This equation will be used later in this study:

$$P_S = P_T \frac{\rho_t A_p}{A_{illum}} \frac{A_{rec}}{\pi R^2} \eta_{sys} \eta_{atm}^2 \tag{15}$$

where P_R is the power recieved, P_T is the power transmitted, ρ_t is the target reflectance, A_p is the projected area of a pixel, A_{illum} is the area illuminated, A_{rec} is the area of the receiving aperture, R is the range to the target, η_{sys} is the overall system's optical efficiency, and η_{atm} is the transmittance through the atmosphere squared to account for the roundtrip path.

One way to use the LADAR range equation is to calculate an atmospheric transmission threshold required for adequate signal. Since there are various types of detectors suitable for direct detection LADAR, that threshold will depend on the type of sensor used. To apply the range equation effectively, it becomes necessary to understand which detector is being used. Of particular interest are avalanche photodiodes which are capable of detecting low signals.

2.3 Detectors

Since direct detection LADAR requires TOF data, conventional cameras that continuously record light intensity are not sufficient. Specialized detectors that can time stamp returns become necessary.

Many detectors useful for LADAR make use of the photoelectric effect. The photoelectric effect describes the interaction between photons and electrons. When a photon of sufficient energy strikes an atom, the photon can be absorbed and excite an electron from a lower energy state − the valence band − into a higher energy state − the conduction band (see Fig. 9) [16]. Conversely, when an electron loses energy and drops from a higher energy state, it can release this energy in the form of a photon.

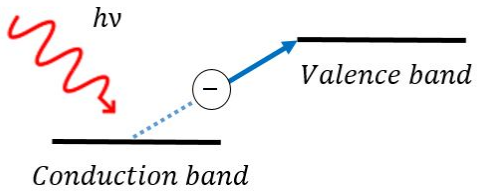

Figure 9. Excitation of an electron by a photon. The photoelectric effect is the basic operating principle for many types of detectors.

Photodiodes, also known as photovoltaic detectors or simply photodetectors, take advantage of the photoelectric effect. When a photon collides with and imparts its energy onto an atom in the photodiode, the electron that gets excited to a higher state also leaves behind a hole where it once was. That hole can be thought of as region of positive charge now that the negatively charged electron is absent. This is known as an electron-hole pair [5]. When an external electric field is applied, as is the case in a photodiode, both the electron and the hole will move, albeit to opposite poles of the electric field. Thus, the photodiode turns photons into current, which can be used as a proxy measure for photons [16]. The current can be found from the

following equation:

$$i_g = \eta \phi_p q \tag{16}$$

where i_g is the photogenerated current, η is the quantum efficiency of the detector in terms of electrons per photons, ϕ_p is the incident photon flux in units of photons per second, and q is the fundamental charge. It is worth nothing that the buildup of holes can be measured as a current as well.

While the electron is accelerating through the material, it is also colliding with the lattice structure of the surrounding material and losing energy. This results in it reaching a saturation velocity. Throughout this collisional process, the electron has the potential to ionize another atom and thereby dislodge an additional electron into the conduction band. This process is known as impact ionization. Both electrons then have the potential to impact ionize further atoms leading to an exponential growth. This resulting cascade of electrons generates a large current and allows for a weak photon flux to be detected by the electronics of the sensor. For this reason, such a detector is known as an avalanche photodiode (APD), a type of photomultiplier [5].

In many cases, the ability to detect a single photon is necessary. Such APDs have been designed and are known as single-photon avalanche photodetectors (SPADs). A common SPAD is the Geiger-mode avalanche photodiode (GmAPD). This is an APD whose electronics are designed such that a single photon will trigger the cascade of electrons necessary to create a detectable current [14]. GmAPDs are different from high gain, linear mode APDs (LmAPD). The difference lay largely in the bias voltage applied to the detectors. A GmAPD is reverse biased past the breakdown voltage to allow an avalanche to occur from a single incident photon. A LmAPD is not as strongly biased resulting in a current that responds linearly to the number of photons received. The detectors used in [12, 13, 14] were all GmAPDs and have proven highly useful in the generation of 3D imagery in the visible and short-wave infrared bands.

Many have also been used in space for range finding.

2.4 Space LADAR Systems

The basic concept of time-of-flight LADAR came around soon after the invention of the laser and was quickly incorporated into space missions. In 1971, as part of the Apollo 15 mission, the US employed a laser altimeter to make topographical measurements of the Moon's surface. Data was limited, however, due to the state of laser technology at the time. NASA used a flash pumped ruby laser that had a pulse rate frequency (PRF) of only 3.75 per minute. For comparison, pulsed lasers with PRFs on the order of hundreds of kHz are now readily available. Between the Apollo 15, 16, and 17 missions, NASA was able to record a few thousand elevation points around the lunar surface [3].

The next laser altimeter NASA launched was the Mars Orbiter Laser Altimeter (MOLA) in 1997 on board the Mars Global Surveyor (MGS). The onboard laser had a PRF of 10Hz − an improvement on the Apollo missions by a factor of 160 [17]. Some useful design parameters for the MOLA are summarized in Table 1.

Tracking range profiles of the Martian surface helped researchers at NASA conclude that the remnants of rivers, deltas, and other hydrological features do exist on Mars [17]. They were able to see them with more detail than previous observation methods had allowed. This lent further evidence to the existence of liquid water on Mars at some point in its history. Additionally, impact craters were documented with much greater detail, improving from a depth resolution of tens of kilometers to ∼100m. By tracking elevation profiles across the planet, they were able to map the planet into 1/64° latitude by 1/32° longitude topographic grids. This corresponds to a $1 \times 2km^2$ grid at the equator.

The same concept of laser rangefinding has been employed around Earth as well

for the purposes of aerosol tracking and arctic ice cap surveying. The Lidar In-space Technology Experiment (LITE), launched in 1994 on STS-64, was used to provide backscattering profiles of various clouds and aerosols using wavelengths of 355nm, 532nm, and 1064nm. The Shuttle Laser Altimeter (SLA) launched twice, in 1996 and 1997, and took measurements of elevation (similar to the MOLA) as well as vegetation coverage. These were the only two LADAR systems to be flown on space shuttles.

Following the space shuttle LADARs, which had to return from orbit, NASA launched multiple Earth-orbiting satellites. The first was the Geoscience Laser Altimeter System (GLAS) aboard the Ice, Cloud, and land Elevation Satellite (ICESat).

ICESat was launched in 2002 for the purpose of monitoring mass and ice changes in Western Antarctica and Greenland. Through elevation mapping of the arctic, ICESat was able to inform researchers that ice caps were receding at rates faster than expected [18]. Similar to previously discussed spaceborne laser altimeters, ICESat operated in the visible and near-infrared (NIR) bands, that is, 532nm for aerosol characterization and 1064nm for altimetry [19]. Researchers found that the GLAS can penetrate optically thin clouds − those which do not attenuate light significantly. The on-board laser was intended to fire continuously, but due to equipment failures its operability was reduced to 4-6 week periods three times annually. It was in operation from 2003-2009. Despite its reduced operability, it made almost 2 billion measurements during its lifetime [20].

The next LADAR system, launched in 2006, was the Cloud-Aerosol LIdar with Orthogonal Polarization (CALIOP) on board the Cloud-Aerosol Lidar and Infrared Pathfinder Satellite Observation (CALIPSO) satellite. Its primary use was in cloud and aerosol characterization [21]. It also operated at wavelengths of 532nm and 1064nm.

ICESat was replaced by ICESat-2 in 2018 which had several improvements on ICE-

Sat. ICESat-2 is equipped with the Advanced Topographic Laser Altimeter System (ATLAS) which splits its laser into six beams in a 3 × 2 grid. This is a significant improvement over GLAS's single laser by giving multiple measurements with each fire. This allowed for improved spatial coverage and slope detection whereas GLAS had difficulty separating elevation change from slope effects. Due to it having multiple transmitters, ATLAS could simultaneously take two parallel measurements in the along-track direction and three parallel measurements in the cross-track direction which allowed for accurate height and slope detections in a single pass [22]. The design specifications for GLAS, CALIOP, and ATLAS are summarized in Table 1.

As with any satellite, cosmic radiation is a major design issue to consider. CALIOP is orbiting at 705km and so it is exposed to harsh radiation. Given that the primary sensor is a photomultiplier, this extra flux can cause enormous increases in noise levels − up to two orders of magnitude. Over time, as a satellite's cumulative dosage of radiation increases, there is a documented increase in dark current which degrades the signal to noise ratio. This has been observed on CALIOP. The increased dosage has also increased the rate at which the laser misfires by producing a pulse with abnormally low energy. These effects remain minimally impactful on the mission and are being remedied through software upgrades [21].

Thus far, the only form of spaceborne LADAR that has been employed is point-to-point range finding for elevation mapping or aerosol characterization. These are

Table 1. Design specifications for previous NASA space laser altimeters.

	MOLA	GLAS	CALIOP	ATLAS
Wavelength (nm)	1064	532, 1064	532, 1064	532
Pulse Energy (mJ)	48	70	110	0.2-1.2
Pulse Length (ns)	8	6	20	< 1.5
PRF (Hz)	10	40	20.16	10 000
Telescope diameter (m)	0.5	1	1	0.8
Field of View (μrad)	850	500	100	< 35

one-dimensional LADAR systems in that the only dimension they document is range. These measurements are mapped to locations on Earth's surface through GPS, not through imaging. No current space LADAR systems have direct 3D imaging capabilities. This is due in part to the fact that the atmosphere can variably attenuate laser signal and therefore present a significant design challenge. In order to understand the hurdles a spaceborne 3D LADAR faces, it is necessary to understand light propagation through the atmosphere.

2.5 Atmospheric Propagation

After two years of the MGS flying around Mars, researchers found that almost all of the missing returns were attributed to atmospheric effects rather than equipment malfunction. The presence of clouds had at times entirely blocked the laser pulse and resulted in no returns [23]. This speaks to the importance of understanding atmospheric effects on laser propagation.

Light propagation through a homogeneous media can be generally described by Beer's Law:

$$\tau_t = e^{-\beta_e z} \tag{17}$$

where τ_t is the transmission ratio, β_e is the extinction coefficient in units of inverse length, and z is the thickness of the medium.

Extinction is the combined effect of light being absorbed and scattered by the medium:

$$\beta_e = \beta_a + \beta_s \tag{18}$$

The absorption coefficient is further defined by the medium's complex index of

refraction, κ, at each wavelength, λ [24]:

$$\beta_a = \frac{4\pi\kappa}{\lambda} \tag{19}$$

There are two theories to describe atmospheric scattering depending on the size of the scattering particle, and both assume spherical scatterers. The spherical particle assumption is not often physically true but does help yield realistic results. When the size of the particle is comparable to or larger than the wavelength of radiation, scattering is described by the Mie scattering theory. When the size of the particle is significantly smaller than the wavelength of radiation, scattering is described by the Rayleigh scattering theory, which helps greatly simplify the scattering expressions. The Rayleigh scattering coefficient can be modeled by [25]:

$$\beta_s = \frac{64M\pi^5 a^6}{3\lambda^4}\left|\frac{n^2-1}{n^2+2}\right|^2 \tag{20}$$

where M is the number of scatterers per volume, a is the radius of the spherical scatterer, and n is the index of refraction of the medium.

It follows, then, that the extent to which light will be absorbed or scattered by the atmosphere depends largely on the wavelength and medium constituents. Figure 10 shows spectral transmission through the atmopshere due to varying molecular constituents. For LADAR based bathymetry, green laser light is often used because it has minimal attenuation in water [2]. In the atmosphere, wavelengths between 5.5-7.5μm are almost completely attenuated due to absorption by water molecules [26].

Atmospheric attenuation and weather create complex effects on radiation propagation and need to be well understood for LADAR system design. To that end, several radiative transfer models have been developed that take into account extinc-

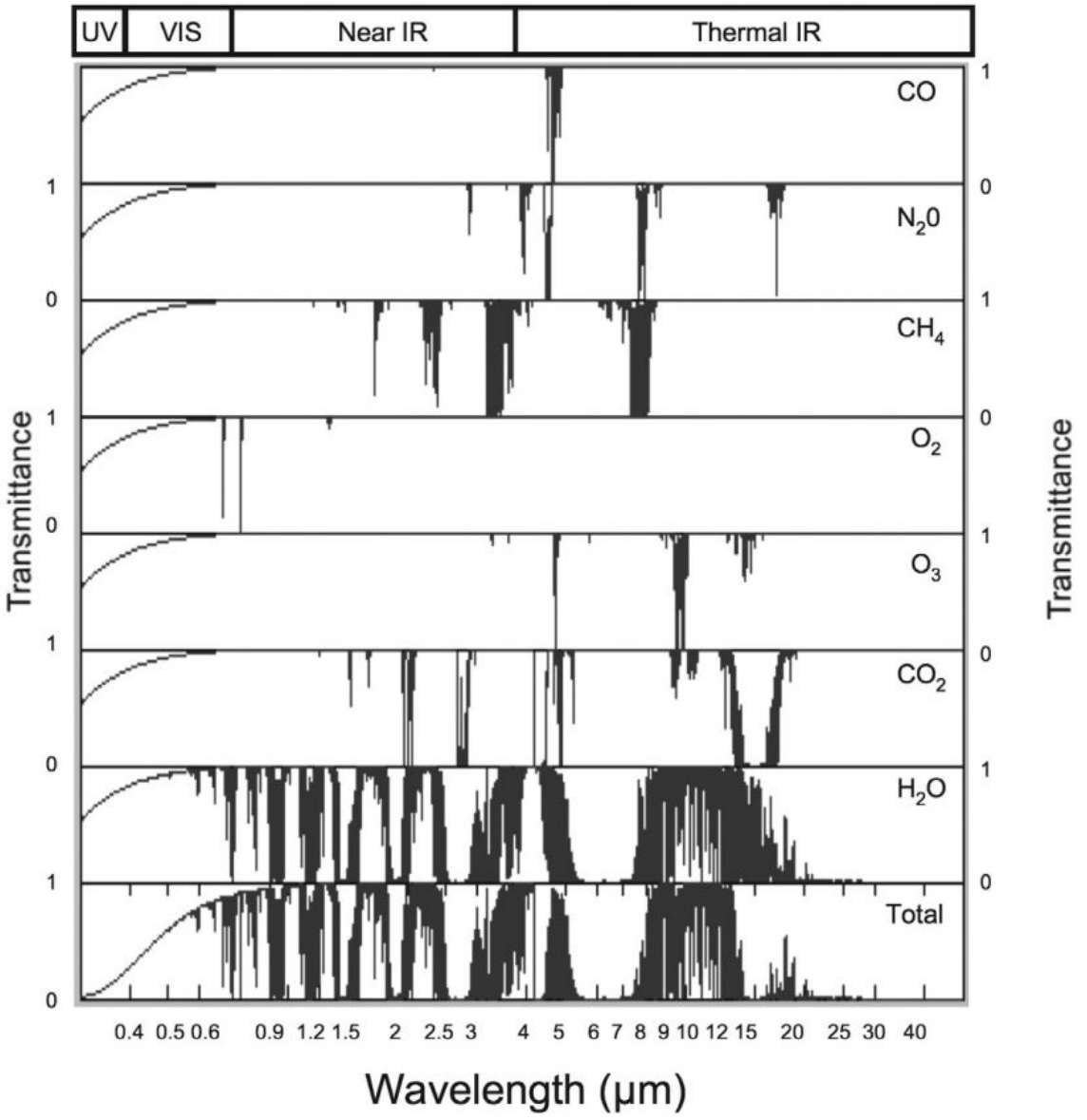

Figure 10. Zenith spectral transmission and absorption due to different molecular constituents. This plot is characteristic of mid-latitude, summer conditions. Courtesy of [26].

tion profiles, weather, and optics to predict system performance. One such simulation is the Air Force Institute of Technology Center for Directed Energy's (AFIT/CDE) Laser and Environmental Effects Definition and Reference (LEEDR) model. LEEDR is an atmospheric effects and radiative transfer code based on first-principles. It is a model that can simulate light propagation anywhere in the world from the ground up to 100km in altitude for a variety of weather conditions. It is capable of simulating any wavelength from 0.355μm up to 8.6m [27]. This model has two primary purposes: 1) to create physically realizable vertical profiles of meteorological data and environmental effects, optical turbulence, and cloud-free line of sight; 2) to provide graphical access and export of probabilistic data from the Extreme and Percentile Environmental Reference Tables (ExPERT) database which contains 573 locations globally (see Fig. 11). Each ExPERT site has an associated probabilistic climatology which can be divided into three hour portions of the day for both summer and winter conditions.

LEEDR has access to historical weather data and can simulate standard conditions for varying locations, seasons, and times of day. Alternatively, it can also be coupled with numerical weather predictions (NWP) which provide the model with gridded weather observations or real-time weather forecasts. NWP are global weather forecasts that take into account observations from various sources: ground observatories, satellite imagery, weather radar, measurements made on aircraft, and others.

LEEDR can take NWP and create four-dimensional weather cubes. These weather cubes define meteorological and multi-spectral atmospheric effects for a given latitude, longitude, and altitude of interest [28]. Given a wavelength of light and its transmittance path, LEEDR can incorporate weather cubes to calculate both the propagation of the light as well as a profile of the atmosphere.

Additionally, LEEDR can leverage more information than is present in NWP. It

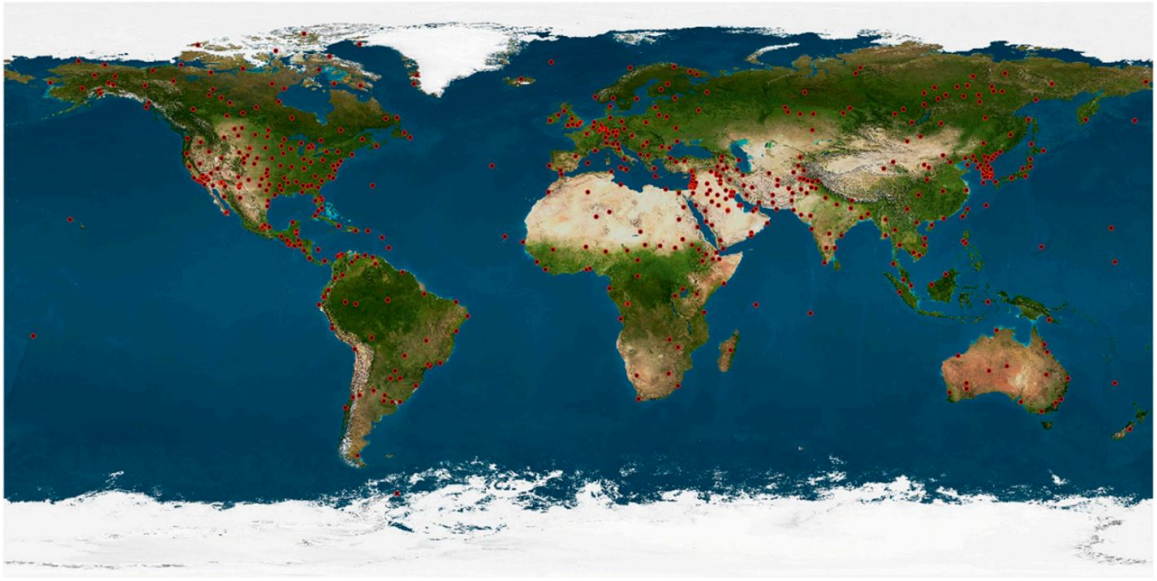

Figure 11. The 573 ExPERT land locations available in LEEDR shown as red dots.

contains a Mie scattering model and the worldwide Global Aerosol Dataset (GADS) aerosol climatology. GADS is a rain and cloud physical model which allows LEEDR to incorporate aerosol optical properties and concentrations. This data is not contained within NWP but since LEEDR acts as a nexus for several data sets, this information can be used to comprehensively describe extinction effects [29].

Studies have been conducted to validate LEEDR. In one study, researchers evaluated the models ability to create atmospheric profiles up through the boundary layer by comparing its performance to real data captured by radiosondes. The simulation was run twice. In one run, LEEDR was passed true, measured surface observations of pressure, temperature, and moisture content. In the other, LEEDR was passed its standard climatological values based on historical data. The objective was to see if custom inputs yielded more accurate results. The findings showed that the root-mean-square error (RMSE) between the model output and the radiosonde data was lower when customized inputs were passed for ground observations as opposed to using historical climatological data for the same season and time. For a winter profile,

the RSME was reduced by 1.8-2.5% while for summer profiles the error was reduced by 20-25% [27]. These findings indicate that LEEDR is capable of characterizing the atmosphere accurately when passed ground observation data. Coupling ground observations with LEEDRs simulation capability can aid in the modeling of high energy laser (HEL) propagation.

The atmosphere modulates laser propagation by subjecting it to turbulence and thermal blooming. Turbulence is the fluctuation in the air's index of refraction caused by irregularities in the atmosphere's temperature and pressure. Thermal blooming is the tendency for high energy lasers to heat the surrounding air through which they are propagating, thereby changing its refractive index [26, 30]. This can have a lensing effect on the beam, causing it to focus/defocus and deviate from its path. Another model created by the AFIT/CDE, which takes these effects into account, is the High Energy End-to-End Operational Simulation (HELEEOS) model.

HELEEOS is an expansion of LEEDR, so it retains LEEDR's functionality, but has a primary focus on modeling directed energy performance. It adds the ability to track a beam profile through the atmosphere and to simulate force-on-force engagements for HEL scenarios. It incorporates the Adaptive Optical Compensation of Thermal Blooming (AOTB) model and the Scaling for High Energy Laser and Relay Engagement (SHaRE) code which uses wave optics simulations to include thermal blooming, turbulence, and diffraction effects [30]. Wave optics simulations alone have high fidelity as they are rooted in physical optics but are computationally intensive. HELEEOS efficiently incorporates wave optics code while retaining computational efficiency. Researchers compared HELEEOS performance to a purely wave optics simulator's performance and reductions in computational time in excess of 99% [30].

One of HELEEOS's key distinguishing features is the ability to estimate power-in-the-bucket (PIB). The PIB represents the total power that is received in a collecting

aperture or that is incident on a target of finite size. LEEDR by itself computes the total laser power transmitted for all space without consideration of a collecting aperture. This is not always realistic, especially over long distances when beams will expand appreciably. HELEEOS, using wave optics code, takes into account the size of the transmitting and receiving optics to estimate the total power that would be measured in a real life scenario.

LEEDR and HELEEOS are capable of incorporating 4D weather cubes by coupling in National Oceanic and Atmospheric Administration (NOAA) gridded NWP data with physical relationships for moisture formation. These weather cubes provide realistic, time varying, cloud free line of sight analytical environments. These have proven useful in analyses of free space optical communications (FSO). FSO operates in SWIR wavelengths which are highly sensitive to the presence of clouds. Employing the 4D weather cubes allowed researchers to understand the probability that a cloud would interfere with an earth-to-space uplink. This enabled them to simulate and analyze bit error rates for a hypothesized FSO system. It was found that atmospheric effects on FSO wavelengths become negligible above 30km but are more pronounced as the lasing angle moves from zenith to the horizon [29]. Incorporating 4D weather cubes provides valuable and realistic predictive capabilities.

While the previously mentioned study focused on SWIR wavelengths, atmospheric studies comparing SWIR and RADAR wavelengths have also been conducted in LEEDR. It is well documented that longer wavelengths, those in the radiofrequency band (RF), tend to penetrate the atmosphere better than shorter wavelengths, such as those in the SWIR. Fiorino et. al. modeled the effects of weather and aerosols on signal-to-noise (SNR) values for hypothetical LADAR and RADAR systems at low altitudes. They evaluated three wavelengths: 1.557μm for LADAR, and 1.2mm (250GHz) and 3mm (95GHz) for RADAR. They found that aerosols are the primary

attenuator of 1-2μm wavelengths for paths traversing the atmospheric boundary layer. Since aerosols are primarily modulated by relative humidity, LADAR performance in the boundary layer is heavily dependent on location and season. Generally, performance worsens in the winter because the cooler temperatures result in higher relative humidities. Similarly, water vapor content is the primary attenuator for the longer wavelengths which makes them less reliable in humid locations and during summer months [31].

The LADAR signal was completely attenuated in the presence of low altitude, stratus clouds, which is a marked disadvantage for LADAR systems. The 1.2mm system was not strongly affected by clouds or fog. The 3mm radar system also performed well in both cloud and fog scenarios and even outperformed the 1.2mm system in humid environments such as the tropics. The RADAR systems show a clear advantage in the presence of clouds. However, simulations were also run for cloud-free, heavy rain conditions. In this scenario, LADAR outperformed RADAR. [31]. The findings showed that performance between LADAR and RADAR systems is highly situationally dependent with neither one having a clear advantage over the other.

As shown in the aforementioned studies, applying laser propagation models can help understand how a LADAR system will perform, but imaging sensors require more than just proper beam propagation. To create useful imagers, high quality and high throughput lenses are needed to clearly resolve targets.

2.6 Non-Traditional Optics

As seen in Equation 6, the resolution of a lens is inversely proportional to its diameter. So in order to create images with high levels of detail, that is, a small resolving angle, either the diameter of the lens needs to be increased or the wavelength

needs to be reduced. For the case of a fixed wavelength LADAR system, only the diameter can be adjusted. Though, for many space-based applications, the size of the optic is limited due to size and weight constraints of satellite payloads. This means that there is an upper weight limit that the optic can be expanded to.

In order to increase size further without increasing incurring weight penalties, gradient index (GRIN) lenses can be employed. In order to understand GRIN lenses, it is necessary to understand how conventional lenses bring light to focus.

A conventional, glass lens has a refractive index that is fixed throughout its volume. The shape of the lens then dictates how and where it will focus light. Considering Snell's Law (Equation 21), parallel rays that enter a spherical lens at its extremities will have a greater angle of incidence than the paraxial rays that enter at the center, and therefore will also be more strongly refracted inside the lens. They will also exit the lens at steeper angles as compared to paraxial rays [4]. Snell's Law is as follows:

$$n_1 \sin\theta_1 = n_2 \sin\theta_2 \tag{21}$$

where n is the refractive index of a material and θ is the angle a ray makes with respect to the surface normal.

A GRIN lens is a lens whose refractive index is a continuous function of position, $n(\mathbf{r})$. Their primary mechanism of focusing light, then, is the changing index itself and not the shape of the lens. This enables them to be made flat and reduce volume. Many manufacturing methods exist, but recently they have started to be produced through quick printing processes. In contrast to conventional lenses, rays passing through a GRIN lens can follow curved, not straight lines. To determine the path the

light will take, Fermat's principle is employed:

$$L = \int_{s_0}^{s} n(\mathbf{r}) ds \tag{22}$$

where ds is a differential length of the path. If the path can be determined by $x(s)$, $y(s)$, and $z(s)$, where s is the length of the path, it can be shown that all three must satisfy the following partial differential equations [5, 32]:

$$\begin{aligned} \frac{d}{ds}\left(n\frac{dx}{ds}\right) &= \frac{dn}{dx} \\ \frac{d}{ds}\left(n\frac{dy}{ds}\right) &= \frac{dn}{dy} \\ \frac{d}{ds}\left(n\frac{dz}{ds}\right) &= \frac{dn}{dz} \end{aligned} \tag{23}$$

or more consicely in vectorial form:

$$\frac{d}{ds}\left(n\frac{d\mathbf{r}}{ds}\right) = \nabla n \tag{24}$$

In the paraxial regime when rays follow paths mostly parallel to the z-axis, the equations in Equation 23 can be simplified to [5]:

$$\begin{aligned} \frac{d}{dz}\left(n\frac{dx}{dz}\right) &\approx \frac{dn}{dx} \\ \frac{d}{dz}\left(n\frac{dy}{dz}\right) &\approx \frac{dn}{dy} \end{aligned} \tag{25}$$

If $n(x, y, z)$ is known, then the two partial differential equations in Equation 25 can be solved for $x(z)$ and $y(z)$ thereby mapping the rays.

Considering a flat, GRIN lens, all parallel rays will enter at the same angle of incidence. However, since the index changes with position throughout the lens, rays will refract at different angles depending on where they strike the lens. By carefully controlling the design of $n(\mathbf{r})$, a lens can be made which focuses light just as a con-

ventional glass lens but with volume savings. GRIN lenses can be printed out of polymers which imply weight saving over glass lenses. For this reason, GRIN lenses are of particular interest for space applications.

III. Methodology

This chapter connects the theory discussed in Chapter II with the work done in this thesis. The research is broken into three components. The theory behind each component is explained first. Then, they are each revisited and the actual methods by which each component was investigated is explained.

The first research component examined is the photon link budget. It is examined in three steps: notional geometric design considerations that lead to a scaling ratio, establishing a photon count threshold, and establishing an atmospheric transmission threshold for the requisite photon count. The purpose of this step is to establish design parameters which can then be passed into models.

The second research component is examining atmospheric transmission models. The models are validated through the use of a transmissometer. The following implementation of those same models is also explained.

The third and final research component is the characterization of non-traditional optics. Methods for analyzing the profile of a laser beam after passing through a lens are explained.

3.1 Theory

Photon Link Budget - Scaling.

Here, a spaceborne GmAPD LADAR sensor is assumed to be orbiting at an altitude of 500km and looking only in the nadir direction.

In order to establish an atmospheric transmission threshold, which is one of the three primary objectives of this research, a photon link budget needs to be established to act as a baseline. Once the link budget is established, atmospheric transmission profiles can be examined in the context of providing sufficient throughput for a space-

borne LADAR.

Three wavelengths are evaluated in this study - 1.06μm, 1.550μm, and 2.134μm. The two longer wavelengths are of particular interest due to the fact that they are more eye-safe. Light at wavelengths below 400nm and beyond 1.5μm are absorbed by water in the eyes [10]. Light in between those wavelengths is focused up to 10^4 times on the retina. While 1.06μm may not be eye-safe, it does provide a clear advantage in its fundamental resolution limit. Referring back to Equation 6, it can be seen that a shorter wavelength corresponds to a smaller resolvable angle. Imaging at this wavelength can provide resolution twice as fine as at 2.134μm.

Equation 15, the LADAR range equation, is essentially a scaling formula. It takes an input and scales it according to the geometry of the application and efficiencies of the system. While the equation has power as that input, measured in Watts, it could easily be another metric, such as photons, without losing any integrity. That is the approach taken in this study. The following calculations will be demonstrated for only one wavelength as the equations hold true for all wavelengths.

Using Equation 1, wavelength is easily converted into energy in units of Joules.

$$E = \frac{hc}{\lambda} = \frac{hc}{1.06\mu m} = 1.88 \times 10^{-19} \frac{\text{J}}{\text{photon}} \tag{26}$$

Then, to get a total number of photons transmitted, the total energy in one pulse must be divided by this photon energy. Given that ATLAS had a laser which was capable of producing 0.2$-$1.2mJ of energy at 1.06μm, it is reasonably assumed that a 2mJ laser is used in this scenario [22].

$$\frac{2 \frac{\text{mJ}}{\text{pulse}}}{1.88 \times 10^{-19} \frac{\text{J}}{\text{photon}}} = 1.07 \times 10^{16} \frac{\text{photon}}{\text{pulse}} \tag{27}$$

The next term in the range equation is $\frac{\rho_t A_p}{A_{illum}}$. Here, as a conservative estimate,

the target is assumed to be Lambertian with a uniform reflectance of 0.1. Since the satellite is aimed at nadir, the projected pixel size can be equated to the ground sample distance (GSD). The GSD is defined here by the as the diffraction limited cross-range resolution as it appears on Earth. Given that ICESat-2 has a 1m diameter telescope, here it is assumed that a 2m optic is used by taking advantage of weight and size savings by using a non-traditional optic. To calculate the GSD, the Rayleigh Criterion from 6 is doubled to represent the full width and multiplied by the range to get the full size as it appears on Earth. The following result is obtained:

$$GSD = 2.44\frac{\lambda R}{D} = 2.44\frac{1.06\mu m \times 500km}{2m} = 0.647m \tag{28}$$

Defining the projected pixel width as the cross-range resolution assumes a diffraction limited system. Assuming square pixels, this corresponds to a projected pixel size of 0.421m^2.

The area illuminated by the laser takes some more calculation. The beam will diverge as it propagates through space due to diffraction. It is assumed that the propagated light travels as a single mode, Gaussian beam transmitted through a circular aperture. With these constraints in mind, the half angle beam divergence for a large propagation distance can be calculated by [9]:

$$\Delta\theta = \frac{\lambda_0}{\pi n w_0} \tag{29}$$

where λ_0 is wavelength, n is the index of refraction of the propagating medium (here assumed to be 1 for air), and w_0 is the beam waist. Using the small angle approximation, which is valid over large distances, the radius of the spot size quickly simplfies to Equation 13:

$$
\begin{aligned}
r &= \Delta\theta z \\
&= \frac{\lambda_0 z}{\pi n w_0}
\end{aligned} \tag{30}
$$

where z is the propagation distance, which is 500km.

Here, the beam is assumed to be expanded to a waist w_0 of 100mm. This yields a half angle beam divergence of ∼6.75 µrad which in turn illuminates a circle with radius 3.37m and area 35.7m^2 at range. It is important to note that this is a slight underestimate as the laser power will exponentially decay as it moves away from the center of the footprint. For the purpose of this analysis, all laser power will be treated as being focused in this circle, meaning the estimated return will be slightly higher than in actuality.

The third term in the range equation is a ratio of the area of the receiver to the hemisphere into which the target will radiate, $\frac{A_{rec}}{\pi R^2}$. This is a straightforward calculation given the previous assumptions that the telescope has a 2m optic and the altitude is 500km. This term evaluates to 4×10^{-12}.

The fourth term is the overall system efficiency. This encompasses the transmission efficiencies and losses from all optical components. This number varies depending on every system. For the purposes of this analysis, it is assumed to be 0.85.

The fifth and last term is the atmospheric transmission coefficient. This number is squared to represent the roundtrip path a laser pulse would take through the atmosphere. Given all other variables and a threshold signal photon count required, a minimum atmospheric transmission can be solved for.

Combining these ratios together and calling it γ, as well as changing the Range Equation to consider photons, the equation can be simplified to:

$$
Ph_R = Ph_T \gamma \eta_{atm}^2 \tag{31}
$$

where Ph_R and Ph_T are received photons and transmitted photons, respectively, and $\gamma = 3.97 \times 10^{-15}$. Thus, all that remains is to establish a minimum photon count and then the atmospheric transmission can be solved for.

Photon Link Budget - Photon Threshold.

Photons do not arrive to detectors at a consistent rate. While the average rate may be constant, the timing of individual photons varies. This uncertainty in the photon arrival time is known as shot noise [16]. There are many other types of noise that contribute to a signal. Some examples include Johnson noise, also known as thermal noise, which is caused by thermally excited electrons triggering detection events; generation-recombination noise which is due to fluctuations in the rates of generation and recombination of electron-hole pairs; $1/f$ noise which is dependent on the modulation frequency of a detector. Shot noise is the lowest amount of noise that can be achieved. That is, when all other noise sources have been reduced to their minimum values, shot noise will dominate. For the purpose of this analysis, given low background radiances and well developed thermal controls for satellites, the detector is assumed to operate in the shot-noise limited regime.

To establish a minimum photon count, shot noise will need further analysis. Photon arrival can be assumed to follow a Poisson distribution [33]. This means that the mean of the distribution is also equal to its variance. Thus, if the mean number of signal photons is known, the noise can be found directly. This makes for a straightforward signal-to-noise ratio (SNR) calculation:

$$SNR = \frac{\bar{x}}{\sqrt{\sigma_x}} = \frac{\bar{x}}{\sqrt{\bar{x}}} \tag{32}$$

where $\bar{x}$ is the mean number of photons and $\sqrt{\sigma_x}$ is the square root of the variance, or the standard deviation. For the purpose of this analysis, a SNR greater than 3 is

chosen as the threshold. This means that, at a minimum, 10 photons per pixel per pulse are required to meet this threshold.

Photon Link Budget - Atmospheric Transmission.

Substituting Ph_R in Equation 31 for $\bar{x}$ in Equation 32 and solving yields the following:

$$\begin{aligned} SNR = 3 &= \frac{Ph_R}{\sqrt{Ph_R}} \\ 3 &= \frac{Ph_T \gamma \eta_{atm}^2}{\sqrt{Ph_T \gamma \eta_{atm}^2}} \\ \eta_{atm} &= \sqrt{\frac{9}{Ph_T \gamma}} \\ \eta_{atm} &= 0.46 \end{aligned} \tag{33}$$

Thus, for 1.06μm light and the given design parameters, a transmission efficiency of $\geq$0.46 is required to maintain a SNR >3.

Repeating the above processes for the longer wavelengths results in lower minimum transmission requirements due to the direct relationship between energy and wavelength. The parameters and results are summarized in Tables 2 and 3.

Parameter	Value	Units
Range	500	km
Telescope Diameter	2	m
Energy/Pulse	2	mJ
Reflectance (ρ)	0.1	unitless
GSD	0.647	m
Projected Pixel Area	0.418	m^2
η_{system}	0.85	unitless
SNR	3	unitless

Table 2. Parameters of the Range Equation that are consistent between all three wavelengths.

Studies have been done to characterize the dark current rate (DCR) in GmAPDs.

Parameter		Value		Units
λ	1.06	1.55	2.134	μm
Energy/Photon	1.88E-19	1.28E-19	9.31E-20	J/Photon
Ph_t	1.07E+16	1.56E+16	2.15E+16	Photons/Pulse
Ph_s	42.38	61.98	85.33	Photons/Pixel
η_{atm}	0.461	0.381	0.325	unitless

Table 3. Parameters of the Range Equation that vary with wavelength.

The dark current is the frequency with which a detector falsely registers photons in the absence of light. It is the sum effect of all noise sources excluding shot noise. It was found that for a 32 by 32 pixel array operated at an average of 248K with an integration time of 2μs, the DCR was 2.2kHz [34]. This procedure was repeated on multiple cameras and the highest measured DCR was 16kHz. Calculating the SNR for the 1.06μm case with this DCR shows that it is negligible in this application and that it is safe to assume shot-noise limited performance:

$$\begin{aligned} SNR_{noDCR} &= \frac{Ph_R}{\sqrt{Ph_R}} = \frac{42.38}{\sqrt{42.38}} = 6.510 \\ SNR_{DCR} &= \frac{Ph_R}{\sqrt{Ph_R + (DCR \cdot \tau_{int})}} = \frac{42.38}{\sqrt{42.38 + (16,000 \cdot 2 \cdot 10^{-6})}} = 6.508 \end{aligned} \tag{34}$$

where τ_{int} is the integration time of 2μs. Clearly, the DCR makes a negligible contribution to the overall noise in this case. This lends validity to the assumption of shot-noise limited operation.

Transmissometers.

It is important to understand how to validate and measure atmospheric transmission. A common and simple device to measure transmission is a transmissometer. A transmissometer is any device that uses light transmission to measure light extinction

along a path in accordance with Beer's Law. They are comprised of a transmitter and a receiver. The transmitter sends out light of a known power and the receiver measures the incident power after propagating through a turbulent path. The ratio of the two powers gives the transmission coefficient. Referencing Equation 17, this can be taken one step further to find the extinction coefficient, β:

$$\begin{aligned} \tau_t &= e^{-\beta_e z} \\ \beta &= \frac{\ln \tau}{z} \end{aligned} \tag{35}$$

where, once again, z is the path length.

Light diffracts as it propagates and so a divergent light source, such as an LED, would broaden and be subject to unwanted scattering due to turbulence as it travels to the receiver. This would result in unwanted light being scattered into or out of the receiver. To circumvent this issue, a collimated source can be employed, such as a laser. While laser beams will still diverge, they can maintain their collimation over much longer lengths than an LED and essentially integrate over atmospheric effects before registering a signal on the receiver. Despite the utility of collimated sources, researchers have made strides in using distributed receive apertures to sample defocused, divergent light to reconstruct beam profiles and estimate path extinction [35]. However, the relatively simple application of Beer's Law stays the same.

Since turbulence is caused by irregularities in the atmosphere's temperature and pressure, the periods of least turbulence are those when the air temperature and pressure are most stable and homogeneous. This is seen at sunrise and sunset, when the air and the surface temperatures equalize and create a temporarily stable environment. Thus, in order to eliminate the effect of turbulence and solely investigate the effect of aerosol scattering and absorption on laser extinction, sunrise and sunset are the best times to take measurements.

Beam Profiling.

One way to examine the quality of a lens is to examine the shape of its focal point and how it comes into and goes out of focus. If a Gaussian beam is sent through an aberration-free lens, then the beam will maintain its Gaussian shape and converge and diverge in accordance with Equation 29. Any deviations from this shape are indicative of aberrations in the lens.

A knife-edge beam profiler is a tool that can measure a beam's width, intensity profile, power, and shape. A knife-edge profiler operates by scanning an aperture with a straight edge over a detector and recording the change in power. Initially, the detector will be completely exposed to the beam. Then the knige-edge of the aperture is scanned across the detector, obscuring the beam. By recording the power with respect to the position of the aperture, a power versus position plot can be made. By differentiating the drop in power with position, the beam shape in the axis of the knife edge's travel can be determined as shown in Fig. 12 .

As the knife edge can only give the beam profile in one dimension (1D), multiple scans at differing angles are required to accurately reconstruct the beam profile. This process is known as reconstructive tomography [36].

Another way to characterize how much aberration a lens has is by computing the MTF. As discussed in Chapter 2.1, the MTF is the modulus of the Fourier Transform of the PSF. The knife-edge profiler gives a detailed spread function at the focus in one dimension, otherwise known as a Line Spread Function (LSF). By taking the Fourier Transform of the LSF and taking the absolute value of the result, the MTF is obtained. The MTF can then be compared to the ideal case to graphically evaluate the quality of the lens.

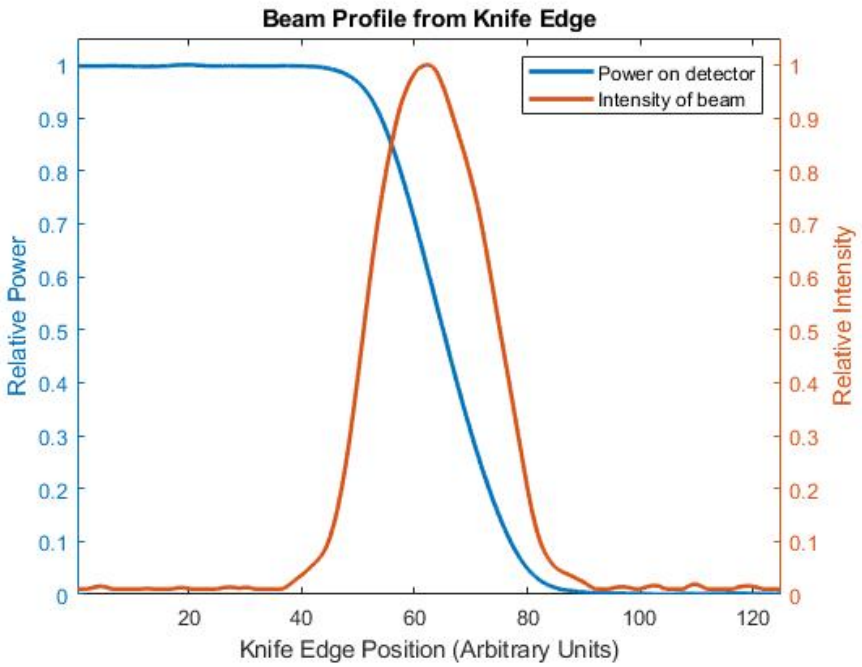

Figure 12. A one-dimensional beam profile as measured from a knife-edge profiler. As the beam scans across the detector, the power will drop, as seen in blue. The rate at which the power drops with position is the beam's intensity profile, as seen in orange.

3.2 Experiment

Model Validation.

Before proceeding with running simulations in LEEDR and HELEEOS, a transmissometer was used to validate the models' performances. To conduct this experiment, laser power was measured at the aperture and then again at range (80-150m) in order to measure the drop in transmission. These measurements were coupled with the following weather measurements: pressure, temperature, relative humidity (PTH), and particle count. These measurements were then input into LEEDR and HELEEOS post-collection to replicate the exact scenario in which the laser was fired. The objective was to compare the simulation outputs to the experimental findings to assess the accuracy of the simulation in predicting laser transmission. As a safety precaution, the laser was always pointed at a negative angle such that it would intercept

the ground slightly beyond the receiver.

The transmitter used was a 1.1mW, 543nm continuous wave (CW) He-Ne laser. The laser was placed on a rail with a 20x magnification, 0.40 numerical aperture microscope objective to expand the beam followed by a 1 inch diameter collimating lens to then collimate the beam (see Fig. 13). The reason for this expansion can be seen in Equation 29. A wider beam will stay more tightly collimated, which is important for transmissometers to get accurate power measurements on receive. The microscope objective was placed approximately 5cm in front of the laser aperture and immediately against the collimating lens. This entire apparatus was placed on a tripod for mobility.

The receive apparatus was placed on a separate rail and tripod. The first optical element on it was a 2 inch diameter lens with a 150mm focus. A Newport 818-SL Photodetector was placed at the focus without any attenuators (see Fig. 14). The photodetector is made of silicon and is sensitive to wavelengths 400-1100nm with a calibration uncertainty of 1%. The detector has a $1cm^2$ active area [37]. The small active area creates the need for the focusing lens. Behind the photodetector was a Newport 1815-C Power Meter to read out the laser power received. To eliminate background noise, a cardboard shield was placed on top of the receive apparatus (see Fig. 15).

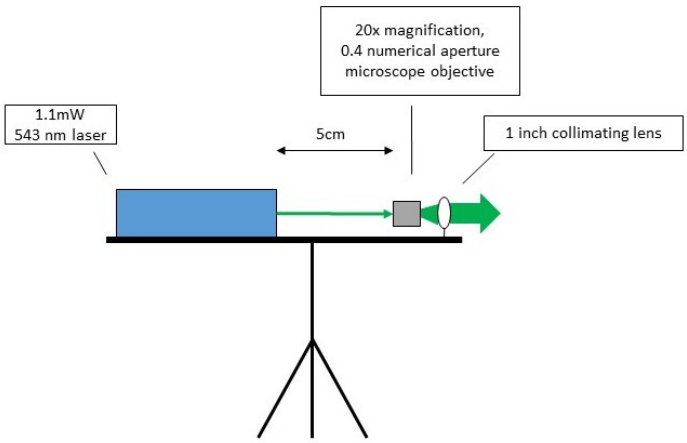

Figure 13. Transmit apparatus. The transmitter is a 1.1mW, 543nm CW laser. Placed 5cm after the exit aperture of the laser is a 20x magnification, 0.40 numerical aperture microscope objective which is placed immediately against a 1 inch collimating lens.

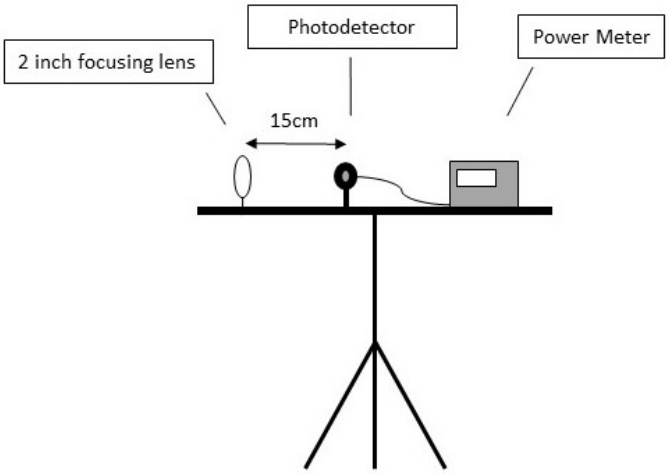

Figure 14. Receive apparatus. A 2 inch diameter lens with a 150mm focus followed by a Newport 818-SL Photodetector at the focus without attenuators followed by a Newport 1815-C Optical Power Meter.

Figure 15. Transmissometer situated for initial reading at Rotary Park. The receive apparatus has a cardboard shield for background reduction. The beam is blocked and the power meter is read off to get a background value, which was zeroed or subtracted from the results post-collection.

Both tripods were placed approximately 150cm above the ground. Prior to measuring laser power, the beam was blocked to measure and record the background flux. The background was either zeroed on the power meter or subtracted from the results post-collection. After a background collection, an initial power reading was taken with the receive apparatus immediately against the transmit apparatus, as shown in Fig. 15. It is assumed that atmospheric losses over the short distance between the rails is negligible. The receive apparatus was then moved 100-150m away and the power was once again recorded at range. Due to the negative pointing angle of the laser, the receive apparatus was approximately 50-130cm off the ground. It was expected that a transmission of 97-99% would be measured at range. This is depicted in Fig. 16. Distance was measured by dropping pins in Google Maps.

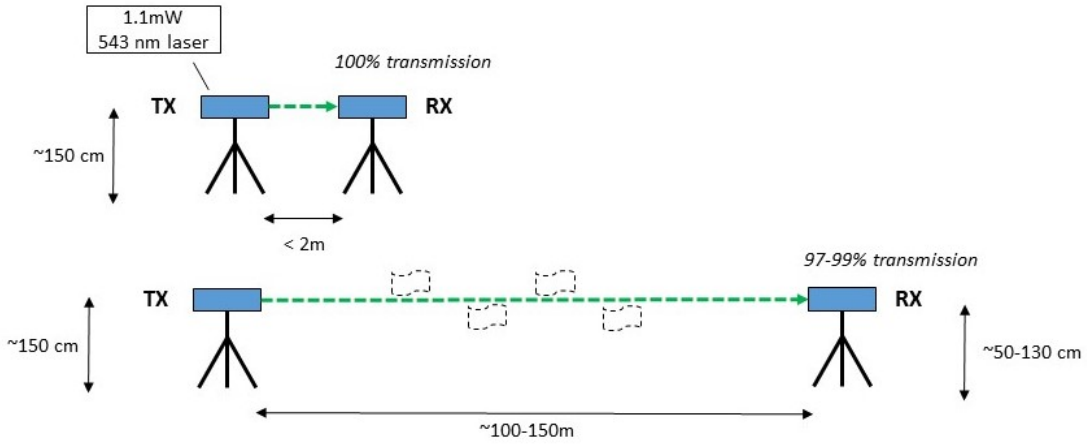

Figure 16. Data collection for the transmissometer. The initial measurement was taken less than 2m from the transmit apparatus, which is treated as 100% transmission. The range measurement is taken 100-150m away where, due to atmospheric attenuation, 97-99% transmission is expected. The receive apparatus is slightly shorter than the transmit due to the negative pointing angle of the laser.

A Kestrel 4000 was used to record PTH concurrently. A Series 200 Modulated Aerosol Growth with Internal water Cycling (MAGIC) Condensation Particle Counter (CPC) was used to measure the concentration of particles 5nm to 2.5μm in size [38].

To investigate the effects of extinction and minimize the influence of turbulence, data was only collected at sunrise and sunset. Data were collected from 14 August 2020 to 16 August 2020 and again from 20 October 2020 to 27 October 2020. Data from 15-16 August were collected at Rotary Park (see Fig. 17a), while 14 August data were collected at Wright-Patterson AFB, Area B (see Fig. 17b). Data from 20-27 October were collected by the Wright-Patterson AFB runway on Area B (see Fig 17c).

(a) Transmisison path at Rotary Park, Beavercreeek, OH.

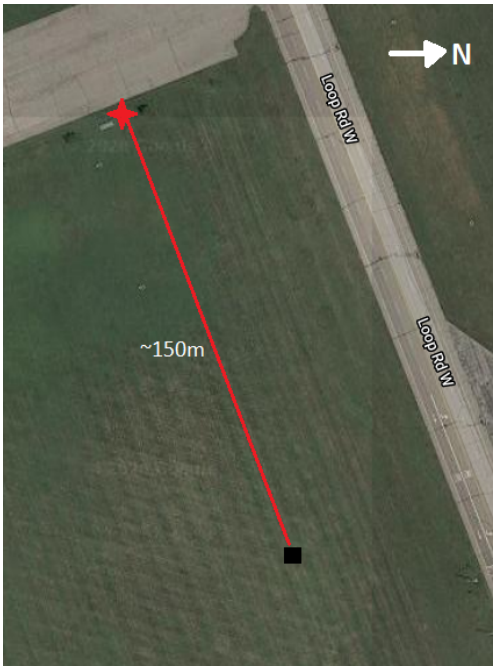

(b) Transmisison path over fields at Wright-Patterson AFB, Area B.

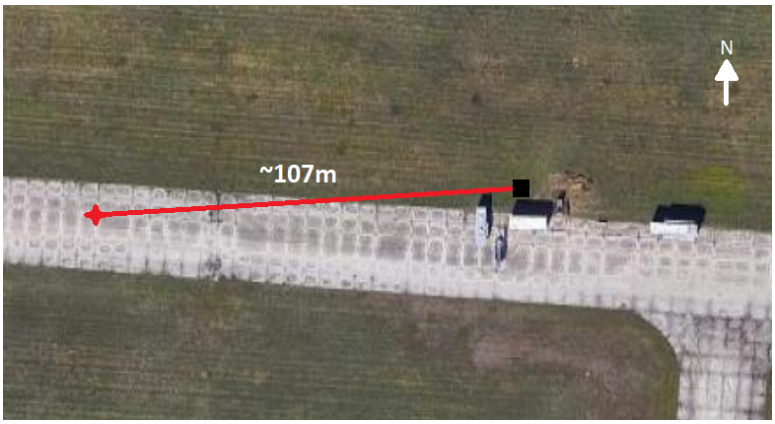

(c) Transmisison path by the runway at Wright-Patterson AFB, Area B.

Figure 17. Experiment geometry for the three collection sites in August and October. The transmit apparatus, represented by the red star, was placed between 80-150m away from the receive apparatus, represented by the black square. The longest path at Rotary Park was ∼130m, the longest path at WPAFB was ∼150m in August and ∼107m in October.

Model Implementation.

After the model validation came model implementation. To evaluate the utility of the proposed direct detect LADAR system, multiple simulations needed to be run.

Each simulation would incorporate historical weather data to predict how often the minimum atmospheric transmission threshold would be met at each location (see the last row of Table 3). LEEDR was used to calculate these predictions.

Weather data is collected four times daily at weather stations across the globe. This data is then fed into models to create NWP which provide PTH, wind, and cloud information. Three of these sites are Yuma, AZ, Wright-Patterson AFB, OH, and Point Barrow, AK. Together these locations represent three different climates: desert, midlatitude, and arctic. These sites were chosen as the subject of this model implementation because the diversity of climates provides insight into how broadly across the globe the proposed LADAR could perform.

This NWP data from 2007-2017, which amounts to ∼15,500 data points, was passed into LEEDR to create weather cubes. Then, LEEDR was executed using these weather cubes to calculate the atmospheric transmission for a vertical path to space. This was done for three wavelengths: 1.06μm, 1.55μm, and 2.134μm. The output was a probabilistic and forecasted atmospheric transmission.

It is important to note that LEEDR is only defined for altitudes up to 100km. It is reasonably assumed that, since the atmosphere is contained well within that upper bound, no laser attenuation occurs beyond 100km. This means that the transmission outputs from LEEDR can safely be applied to a LADAR orbiting at 500km.

Lens Characterization.

Four GRIN optics were obtained from the company NanoVox for testing − three 3 inch diameter lenses and one 15mm diameter lens. Each lens had an index that was constant in depth but gradient radially. The lens parameters are summarized in Table 4. Due to laser availability, only the 15mm lens was used for beam profiling.

In order to characterize the focusing quality of the GRIN optic, a Newport KEP-

Table 4. GRIN lens design parameters. λ is the wavelength the lens was designed for, f_c is the cutoff frequency, n_0 is the index of refraction at the center, and Δn is the total change in gradient from the center to the outside edge with the outside being at the greater value.

λ	1.55	μm	633	nm
Diameter	15	mm	3	inch
Thickness	3	mm	2	mm
f/#	4.8		38.4	
f_c	67.2	cycles/mm	20.6	cycles/mm
n_0	1.5232		1.535	
Δn	0.1131		0.125	

7-IR3 knife-edge profiler was used. The KEP-7-IR3 has an InGaAs detector with a 9mm^2 square active area. It's spectral range is 800-1800nm. There are seven knife-edges on a rotating drum which allow for 1D profiles in seven axes, as depicted in Fig. 18.

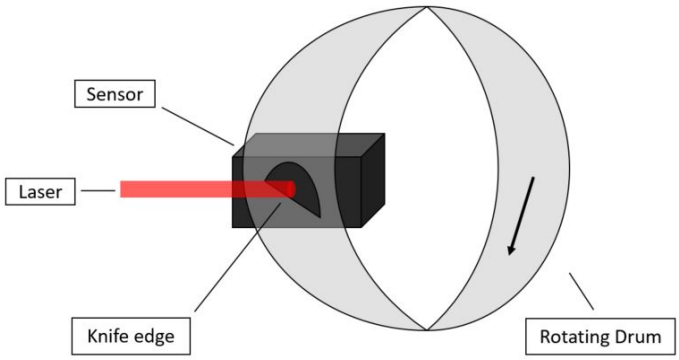

Figure 18. A drum with a knife edge aperture cut out of it rotates and passes over the detector. The KEP-7-IR3 has seven such apertures at varying angles but only one is shown here. This allows for the beam to be profiled in seven different axes.

The profiler itself has two primary axes, V and W, which are situated perpendicular to one another and angled 45° with respect to the base of the detector, as shown in Fig. 19. One-dimensional profiles are outputted with respect to these two axes.

The beam profiler was placed onto a 3-axis stage and mounted to a rail. The micrometers on the stage had 0.001 inch precision. A 10.9mW, 1.55μm fiber laser

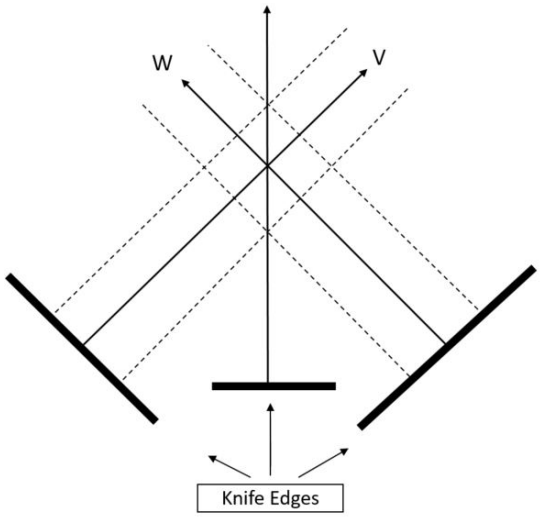

Figure 19. The KEP-7-IR3 has two primary axes, V and W, which run diagonally across the detector. One-dimensional profiles are given with respect to these axes.

was collimated with a 1 inch diameter lens with anti-reflective coating. The shape of the collimated beam was recorded. Then, the GRIN optic was placed at the end of the rail to focus the laser beam. The nominal focus of the beam was found visually using IR card. The beam profiler was placed at this point. Then, the 3-axis stage was used to make fine adjustments while monitoring the output of the beam profiler to locate the point at which the beam width was smallest in one axis. Data was streamed to a nearby laptop via PCI card. The optical setup is shown in Fig. 20

Once the focus was found in one axis, the beam profiler was intentionally translated slightly along the optical axis to spoil the focus and expand the width by approximately 5-15μm. Then, the beam width was recorded. After recording the width at one location, the beam profiler was translated back towards the focus in increments of 0.001 inch with the width being recorded at each increment. Once the beam profiler reached the focus again, the profile of the beam was recorded. Then it was slid further past the focal point to record the increasing beam width as the beam defocused again. Data collection was stopped once the width was approximately equal

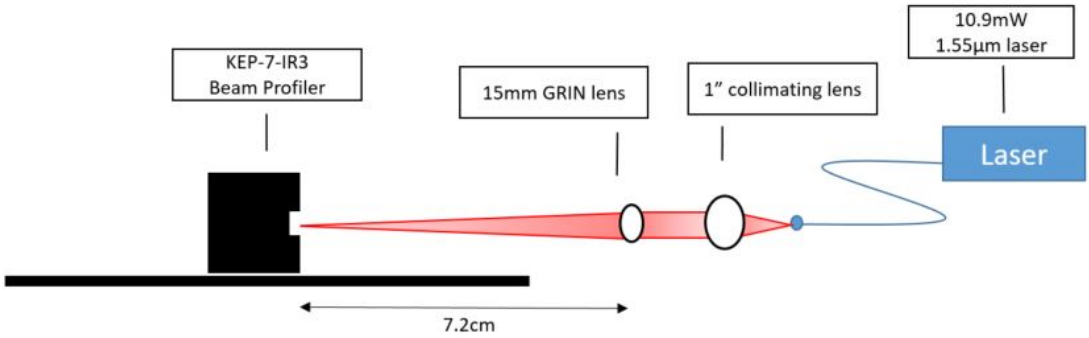

Figure 20. Optical setup for knife-edge beam profiler. The fiber laser is free-space coupled into a 1 inch collimating lens. The collimated light then propagates to the 15mm GRIN lens under test. The beam profiler is positioned at the focus of the lens 7.2cm away.

to the width at the originally spoiled focus. This process was conducted for both the V and W axes.

Since system efficiency is a term in the Range Equation, lens transmission was also measured. An Ophir power meter was placed in front of the collimating lens to record the initial power. Fifteen measurements were taken at one second intervals. Then the GRIN lenses were individually placed in front of the power meter and the process was repeated.

The larger lenses were optically slower than the small lens, that is, they had significantly longer focal lengths with respect to their diameters. This was due to manufacturing constraints. Through Voxtel's manufacturing process, smaller lenses were easier to manufacture than larger lenses. In real applications, as discussed in Chapter 2.1 and Equation 6, larger lenses can increase the resolving ability of an optical system and so large diameters are desirable. To achieve this end despite having slow lenses, the lenses can be stacked against one another to shorten the effective focal length and increase the focusing power. So, as a system consideration, the transmission of the 3 inch lens stack was also measured.

IV. Results and Analysis

This chapter will discuss the results and analysis from the methods described in Chapter III. This chapter follows a similar layout as the previous one. It begins with the results from the atmospheric propagation model validation. These results gave confidence in moving forward with implementing the model. The results from the model implementation are discussed next. The model was run over three different locations using 11 years worth of weather data. This yielded a probabilistic transmission distribution for the different locations. However, the transmission through the atmosphere cannot be viewed alone. A crucial piece in the photon link budget is the overall system efficiency. As such, the last section of this chapter discusses the transmission and overall quality of the GRIN lenses analyzed.

4.1 Transmissometer

For the purposes of this analysis, it is assumed that the PTH and particle count did not vary appreciably throughout the duration of the data collection or between the transmit and receive sites. This is a safe assumption given that the data collections took no longer than one hour each.

The transmission results are tabulated in Tables 5 and 6. Certain dates are missing due to scheduling conflicts. The October collections have three data points taken at noon. This was due to persistent cold and overcast conditions which indicated low turbulence and therefore good data collection conditions.

The fourth column in Tables 5 and 6 represent the difference between the measured value and the model prediction, with the measured value being held as the truth. A negative percentage indicates an overestimate of the model and a positive percentage indicates an underestimate.

The error margins on the measured values were calculated by adding fractional uncertainties in the measurements made at the transmit and receive apertures and multiplying by the measured transmission as adopted by [39]:

$$T = \frac{P_t}{P_r} \tag{36}$$

$$\frac{\sigma_t}{P_t} + \frac{\sigma_r}{P_r} = \sigma_{T-fractional} \tag{37}$$

$$T \cdot \sigma_{T-fractional} = \sigma_T \tag{38}$$

Where P_t and P_r are power measured at the transmit and receive apertures, respectively; σ_t and σ_r are the standard deviations of the measurements taken at the transmit and receive apertures, respectively; and $\sigma_{T-fractional}$ and σ_T are the fractional and overall uncertainties, respectively.

Table 5. Transmission results and corresponding LEEDR simulation outputs.

Date	Avg. Measured Transmission(%)	LEEDR Prediction(%)	Difference(%)
Aug 14 PM	94.8 ± 0.86	99.66	-4.88
Aug 15 PM	94.9 ± 0.50	99.71	-4.77
Aug 16 AM	38.6 ± 2.22	38.08	0.48
Oct 20 Noon	89.9 ± 0.52	99.50	-9.61
Oct 22 PM	91.3 ± 1.25	99.20	-7.86
Oct 23 AM	94.6 ± 1.17	99.30	-4.68
Oct 26 Noon	95.0 ± 0.67	99.70	-4.68
Oct 27 Noon	95.6 ± 0.54	99.80	-4.16
Oct 27 PM	89.1 ± 1.32	99.70	-10.63

Table 5 compares the measured transmissions to the LEEDR predicted values. It was noted that LEEDR consistently and considerably overestimated transmission. Upon further analysis, it became clear that this is due to the fact that LEEDR considers all laser power that is forward scattered into the observer's plane. It does

Table 6. Transmission results and corresponding HELEEOS simulation outputs.

Date	Avg. Measured Transmission(%)	HELEEOS Prediction(%)	Difference(%)
Aug 14 PM	94.8 ± 0.86	91.7	3.1
Aug 15 PM	94.9 ± 0.50	91.3	3.7
Aug 16 AM	38.6 ± 2.22	34.2	4.4
Oct 20 Noon	89.9 ± 0.52	91.5	-1.6
Oct 22 PM	91.3 ± 1.25	91.1	0.3
Oct 23 AM	94.6 ± 1.17	91.2	3.4
Oct 26 Noon	95.0 ± 0.67	91.6	3.4
Oct 27 Noon	95.6 ± 0.54	91.7	3.9
Oct 27 PM	89.1 ± 1.32	91.6	-2.5

not take into account the finite sizes of collecting apertures or the initial beam width. It essentially treats the light source as a point source. LEEDR presents great utility for understanding overall atmospheric transmission for particular wavelengths, but lacks the ability to simulate real laser engagements. HELEEOS, however, does have these capabilities and, as shown in Table 6, generates much more accurate predictions.

HELEEOS's PIB feature considers the "bucket" to be the receiving aperture and the source to be the transmitting aperture. In practice, the source may not take up the full width of the transmitting aperture, and similarly not all light received will necessarily be forward scattered into the receiving aperture. As an approximation, the "bucket" can exchanged for the approximate beam width at the target. This effectively treats the beam size at range as the receive aperture. Similarly, the transmit aperture can be replaced by the beam size at the source. Since the PIB was not considered until after the LEEDR analysis yielded poor results, the size of the beam was not directly measured during data collection. Instead, the beam was approximated as being 1cm wide at the source and 2.5cm wide at the receiver. With these approximations, HELEEOS delivered predictions that were all within <5% of the measured values.

Figure 21. A foggy morning at Rotary Park. The laser can be seen clearly and brightly as viewed from 130m due to off-axis scatter. This is due to the high concentration of fog droplets scattering the light. This resulted in a low transmission of only 38.6%.

Of significant interest is the morning of 16 August when there was a marked decrease in transmission. This morning was particularly foggy (see Fig. 21), while all other mornings, evenings, and noontime collections were under completely clear conditions. This fog caused significant attenuation of the laser beam. Without a nephelometer, which could quantify the fog particles in the air, the fog content had to be estimated for the model. LEEDR and HELEEOS are both capable of simulating various forms of clouds and precipitation. Their default value for fog concentration is $15/cm^3$, which corresponds to a visibility of 350m. That morning, Wright-Patterson AFB reported a visibility of 3/4 mile, approximately 1200m, on Area A. It is reasonable and expected that the surface visibility would vary greatly and potentially be lower at Rotary Park, which is on grassy terrain and is several miles away from the weather station. To compensate for the greater visibility reported on Area A, the default of 15 fog droplets per cm^3 was overridden with $13/cm^3$, which corresponds to a visibility of 410m. This modification to the fog feature resulted in an output

of 34.2%, which is within 4.4% of the measured value. This indicates the versatility and robustness of the models since they are able to accurately accommodate diverse weather conditions.

While promising, these results are only valid at one wavelength, 543nm, which is a pitfall of transmissometers. They only hold true for single wavelength transmission. However, these results do give confidence that HELEEOS can perform with less than 5% error when passed only pressure, temperature, humidity, and particle count and using standard, climatological values for all other variables. The flexibility of the model combined with HELEEOS's <5% error gave sufficient confidence to proceed with the model implementation to evaluate atmospheric transmission at SWIR wavelengths.

4.2 Model Execution

The fraction of instances in which the proposed LADAR system would be able to maintain an SNR >3 is summarized by location and wavelength in Tables 7, 8, and 9. The transmission results showed that overall, Yuma, AZ exceeded its minimum transmission threshold most often. Point Barrow showed the second highest frequency of surpassing the threshold and Wright-Patterson AFB had the lowest.

Wavelength (μm)	1.06	1.55	2.134
Peak Transmission	0.966	0.984	0.981
% above Threshold	53.41	53.47	53.47
% in Zero Transmission Bin	42.72	42.72	42.72
Occurrences from Zero−Threshold	11	10	10
% Above Threshold w/o Zero Bin	99.83	99.84	99.84

Table 7. LEEDR transmission results for Point Barrow. The peak transmission was the highest of all sites at nearly 1. The minimum threshold was met with the lowest frequency of all sites, ∼53%. This is due to the high frequency of 0% transmission days due to clouds. Of the data points that were below the threshold, only 10-11 were not due to clouds. Without clouds, transmission is above the threshold greater than 99.8% of the time.

Wavelength (μm)	1.06	1.55	2.134
Peak Transmission	0.824	0.838	0.836
% above Threshold	58.05	59.41	59.77
% in Zero Transmission Bin	36.36	36.35	36.36
Occurrences from Zero−Threshold	252	232	237
% Above Threshold w/o Zero Bin	96.89	97.14	97.07

Table 8. LEEDR transmission results for WPAFB. The peak transmission for all wavelengths was >0.82. The minimum threshold was only met 58-59% of the time, markedly lower than at Yuma. Of the three wavelengths, 1.55μm had the highest performance peak transmission but 2.134μm surpassed the minimum threshold most frequently. Of the data points that were below the threshold, only 237-252 were not due to clouds. Without clouds, transmission is above the threshold greater than 96.5% of the time.

Wavelength (μm)	1.06	1.55	2.134
Peak Transmission	0.855	0.868	0.866
% Above Threshold	84.16	84.44	84.48
% in Zero Transmission Bin	12.35	12.34	12.34
Occurrences from Zero−Threshold	40	38	37
% Above Threshold w/o Zero Bin	99.61	99.63	99.64

Table 9. LEEDR transmission results for Yuma. The peak transmission for all wavelengths was >0.85 and the minimum threshold was met >84% of the time. Of the data points that were below the threshold, only 37-40 were not due to clouds. Without clouds, transmission is above the threshold greater than 99.5% of the time.

The distributions can be seen in the following probability distribution functions (PDFs) which are divided into 40 bins each representing 0.05, or 5%, wide increments in transmission (see Figs. 22−24).

Of the three wavelengths, 1.55μm has the highest peak transmission. Despite it having the highest peak transmission, 2.134μm tended to pass the minimum transmission threshold with the greatest frequency, albeit marginally.

While the threshold was passed at varying rates between the sites, performance was highly consistent between wavelengths. The threshold passing rate varied by no more than 1.58% between wavelengths. It appears that the location, not the wavelength, was the primary discriminating factor in acquiring sufficient laser transmission.

This requires the differences in the locations to be scrutinized. Upon examining the PDFs, some clear differences can be understood. Point Barrow had the largest fraction of occurrence in the 0-2.5% transmission bin at 42.72%. Similarly, at WPAFB there was a 36.36% chance of having 0-2.5% transmission. Yuma, however, had the lowest chance of exhibiting transmission that low at only 12.34%. Out of all the instances that had below threshold transmission, the 0-2.5% bin held the greatest share. These low transmissions are due to cloud cover. This leads to the conclusion that a location's primary cause for insufficient SNR will be cloud cover.

To further investigate this, the third row of Tables 7, 8, 9 records the number of data points that were above 2.5% but below the threshold. These numbers represent the number of simulations that resulted in below threshold transmission but were not due to cloud cover. No more than 252 out of the ∼15,500 data points per run fell in this category. This means that, when clouds are not present, the threshold transmission was met at least 96% of the time, as summarized in the fifth row of the aforementioned tables.

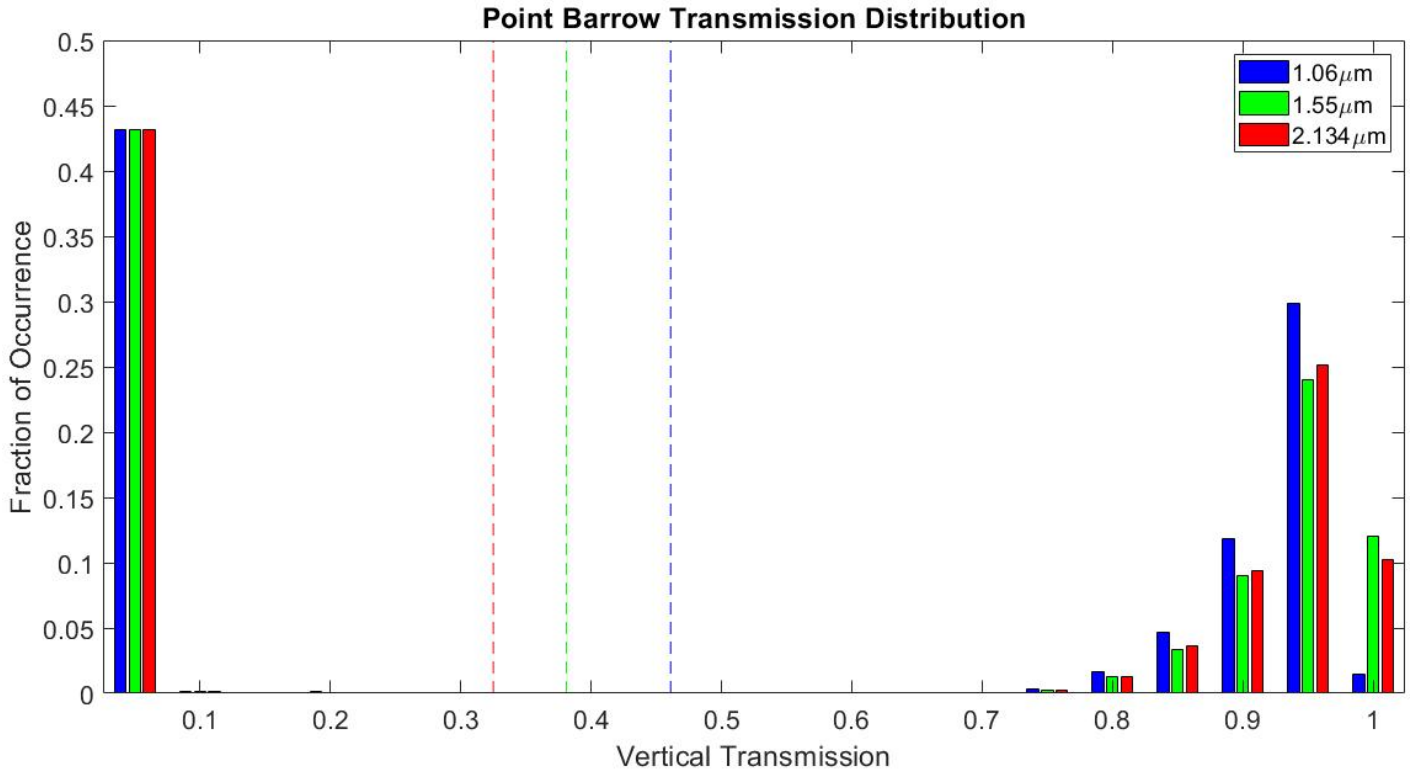

Figure 22. The transmission distribution at Point Barrow is shown here. The dashed lines represent the threshold transmission values for each wavelength. 1.06μm shows a peak transmission of 0.966 and surpasses the 0.461 minimum transmission threshold 53.41% of the time. 1.55μm shows a peak transmission of 0.984 and surpasses the 0.381 minimum transmission threshold 53.47% of the time. 2.134μm shows a peak transmission of 0.981 and surpasses the 0.325 minimum transmission threshold 53.47% of the time.

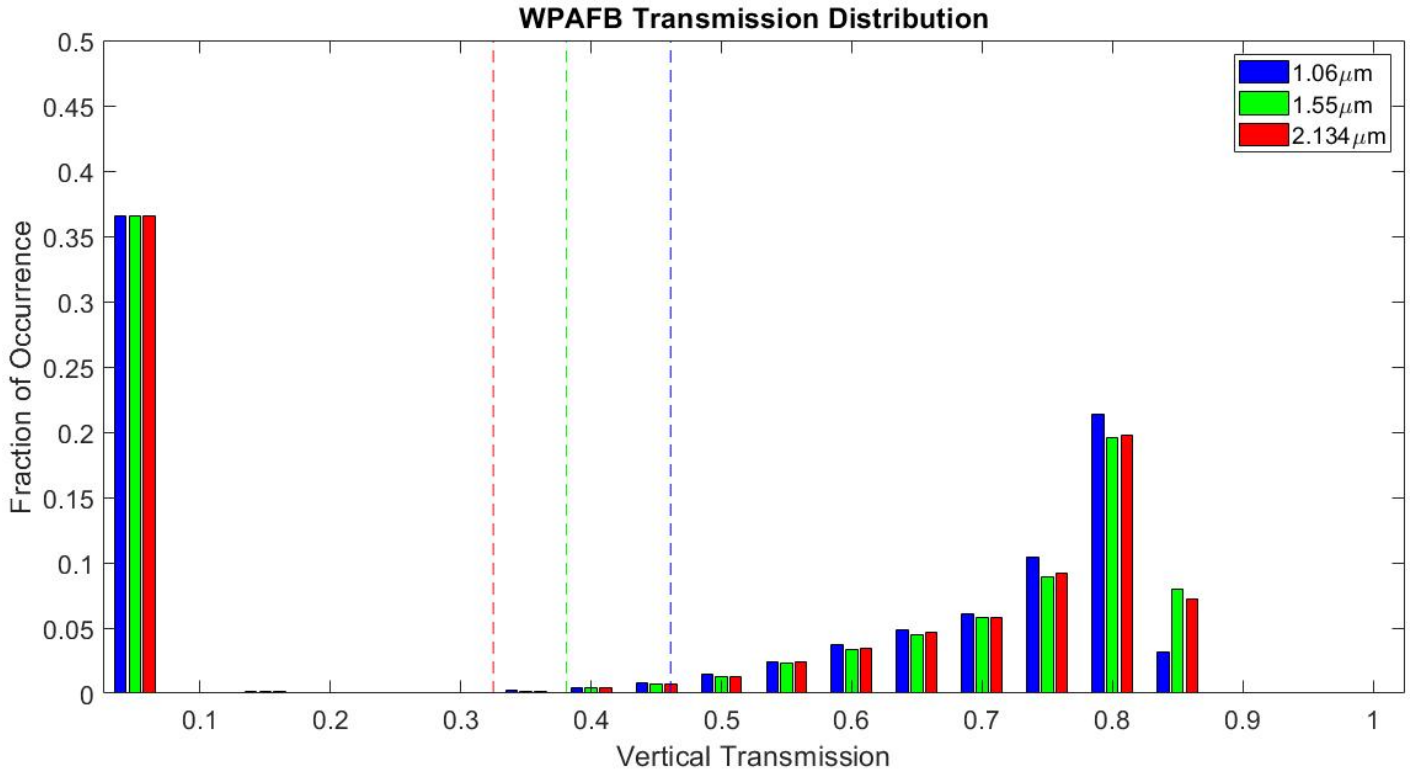

Figure 23. The transmission distribution at WPAFB is shown here. The dashed lines represent the threshold transmission values for each wavelength. 1.06μm shows a peak transmission of 0.824 and surpasses the 0.461 minimum transmission threshold 58.05% of the time. 1.55μm shows a peak transmission of 0.838 and surpasses the 0.381 minimum transmission threshold 59.41% of the time. 2.134μm shows a peak transmission of 0.836 and surpasses the 0.325 minimum transmission threshold 59.77% of the time.

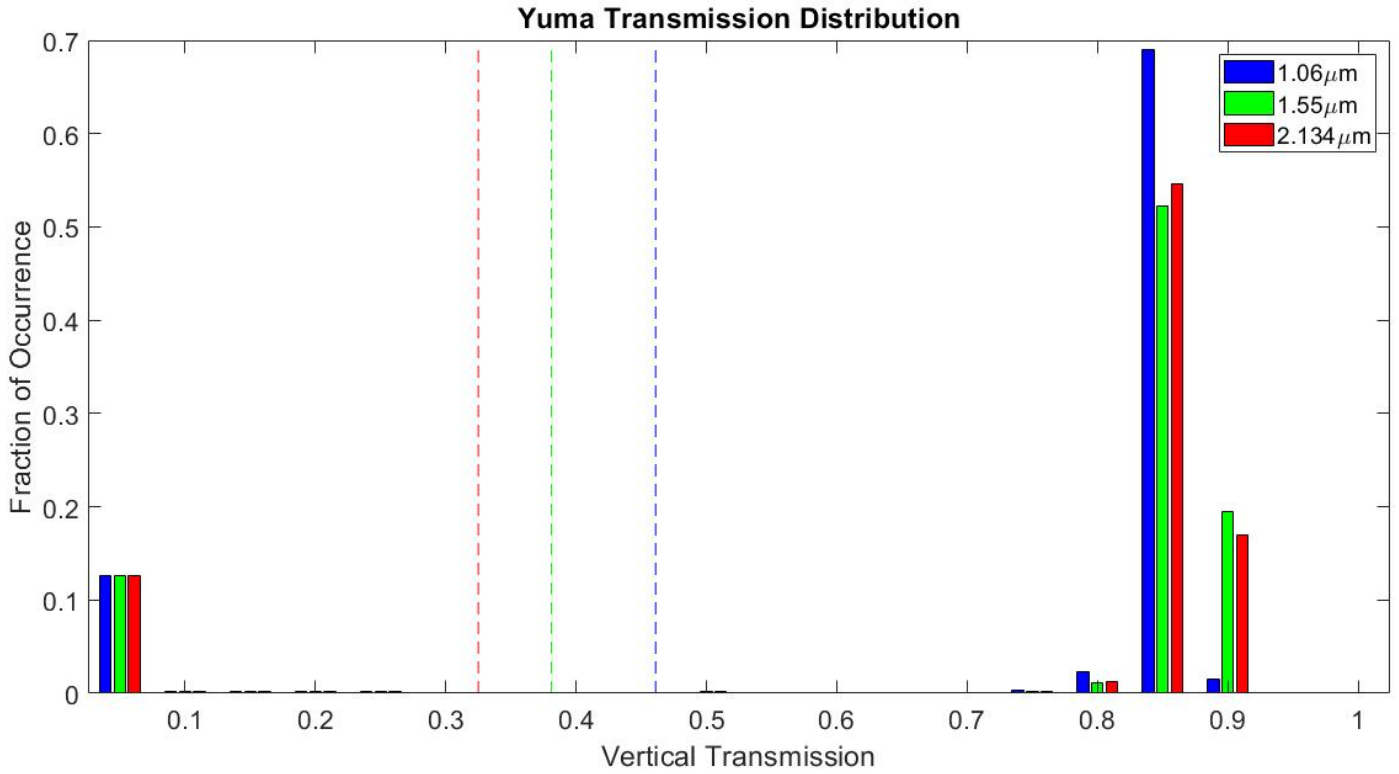

Figure 24. The transmission distribution at Yuma is shown here. The dashed lines represent the threshold transmission values for each wavelength. 1.06μm shows a peak transmission of 0.855 and surpasses the 0.461 minimum transmission threshold 84.16% of the time. The transmission distribution at Yuma for 1.55μm shows a peak transmission of 0.868 and surpasses the 0.381 minimum transmission threshold 84.44% of the time. 2.134μm shows a peak transmission of 0.866 and surpasses the 0.381 minimum transmission threshold 84.48% of the time.

An interesting finding was that Point Barrow had a higher peak transmission WPAFB but did not exceed the minimum threshold as often as WPAFB. Closer examination of the PDFs for WPAFB reveals more information (see Fig. 23). The reason for WPAFB exceeding its threshold more often is that it was less affected by cloud cover. Additionally, across all wavelengths, the PDFs show a markedly longer tail that followed the peak transmission. While most of the data points in the tail were above the minimum threshold, it indicates that something is inherently different about the atmosphere above WPAFB that causes increased attenuation.

This difference is that WPAFB, by climatology, is expected to typically have a higher concentration of aerosols and relative humidity than either Yuma or Point Barrow. Relative humidity increases dramatically in the boundary layer with increasing altitude. This in turn increases the sizes of water-soluble aerosols due to water uptake, which then increases scattering [40]. A thick, humid boundary layer, then, will attenuate more signal than a thin one. The difference in the depths of the boundary layers is apparent in Figures 25, 26, and 27. Yuma tends to have a thicker boundary layer than WPAFB, but the humidity is significantly higher at WPAFB, hence the attenuation. Evidently, humid locations will exhibit a wider distribution of transmissions than less humid locations. This is an important consideration in making active sensing systems.

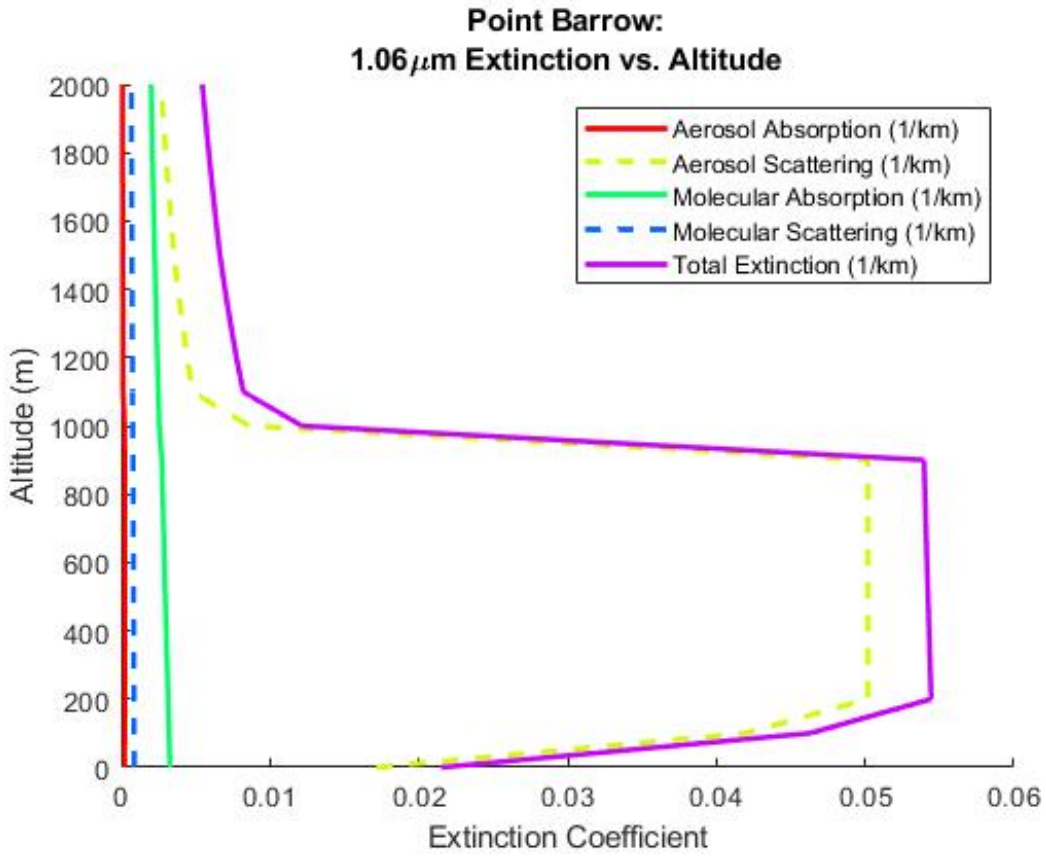

Figure 25. Extinction vs. altitude for 1.06μm light at Point Barrow for a summer atmosphere between the hours of 0600-0900. This figure indirectly shows the thickness of the boundary layer above Point Barrow. The lines depict extinction per kilometer of altitude for 1.06μm light. The bulge to the right represents a region of significant extinction which is due to the boundary layer.

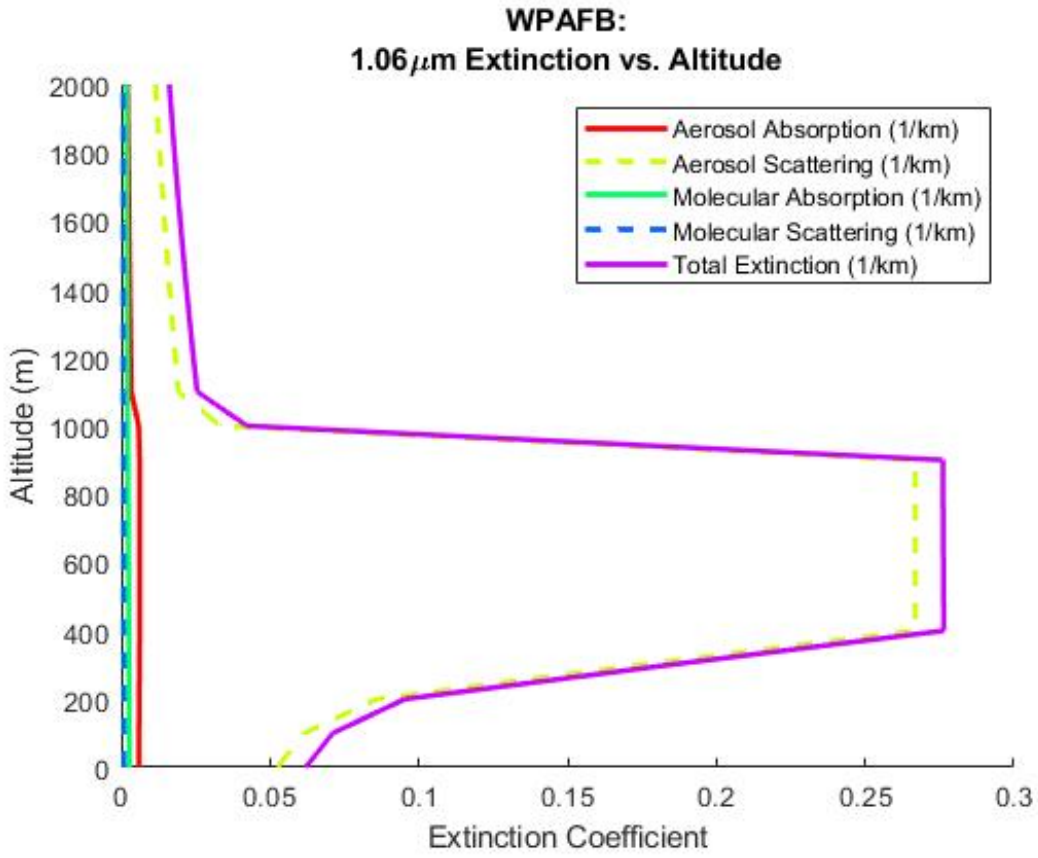

Figure 26. Extinction vs. altitude for 1.06μm light at WPAFB for a summer atmosphere between the hours of 0600-0900. This figure indirectly shows the thickness of the boundary layer above Point Barrow. The lines depict extinction per kilometer of altitude for 1.06μm light. The bulge to the right represents a region of significant extinction which is due to the boundary layer. Note the scale of the horizontal axis is much larger than the extinction plots for Yuma or Point Barrow.

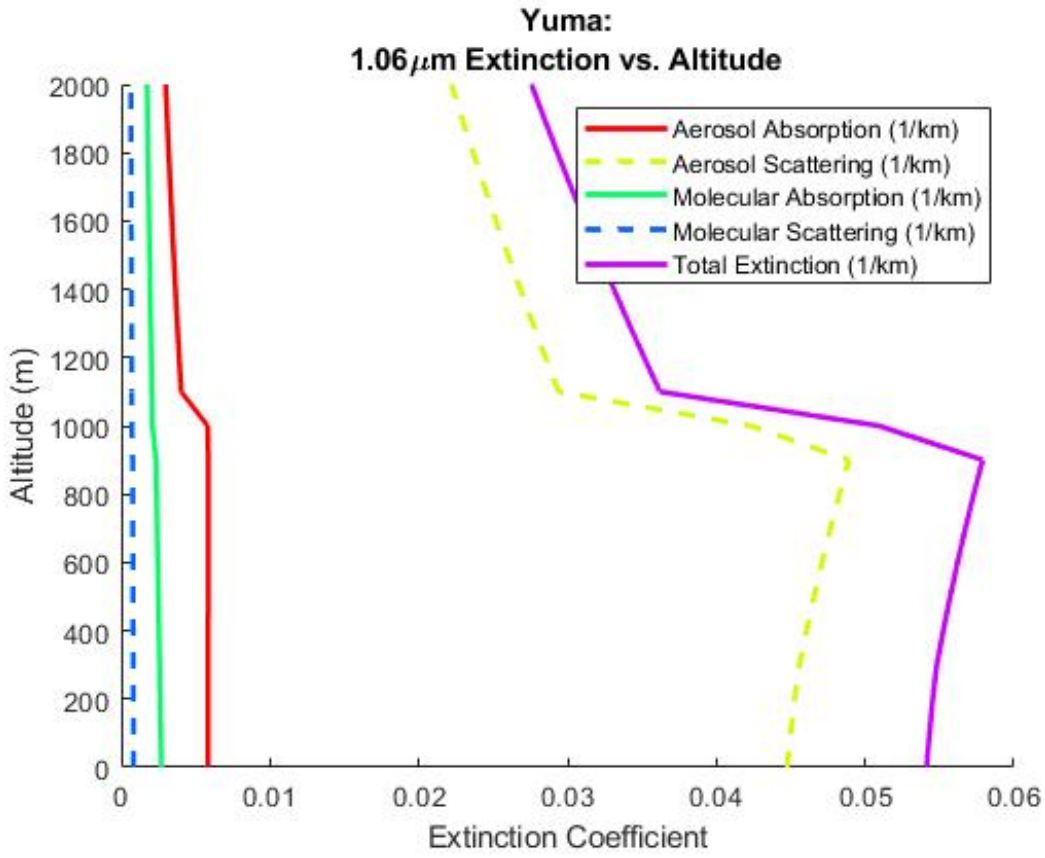

Figure 27. Extinction vs. altitude for 1.06μm light at Yuma for a summer atmosphere between the hours of 0600-0900. This figure indirectly shows the thickness of the boundary layer above Point Barrow. The lines depict extinction per kilometer of altitude for 1.06μm light. The bulge to the right represents a region of significant extinction which is due to the boundary layer. While the boundary layer is thickest here as compared to WPAFB or Point Barrow, the horizontal scale shows the extinction in the layer is minimal. This is due to low humidity.

4.3 GRIN Lens Characterization

The transmissions of the four GRIN lenses are summarized in Table 10. Three measurements have no associated error. This was due to stable power output during the duration of the collection. While the 3 inch diameter lenses were designed for optimal throughput at 633nm, they were tested at 1.55μm to push the bounds of the technology and see if they might hold some utility at relevant wavelengths. The lens manufacturer calculated a ≈4.5% Fresnel reflection from the surface of the

Table 10. Transmission values of GRIN optics.

Lens Diameter	Transmission
15mm	0.899 ±0.001
3" Lens 1	0.830
3" Lens 2	0.828
3" Lens 3	0.829 ±0.001
3" Lens Stack	0.586

lenses. This was valid for wavelengths between 440-1005nm for the 3 inch lenses, and wavelengths centered on 1.55μm for the 15mm lens. To push the limits of the 3 inch lenses, they were also tested at 1.55μm along with the 15mm lens. Assuming the Fresnel reflectance holds at this wavelength, the total expected transmission, neglecting absorption, is reduced to 0.912. This is considering both of the air-to-lens interfaces. This implies the 15mm lens and Lens 1 absorb 0.013 and 0.082 of the total light intensity, respectively. If the lenses can be coated with anti-reflective coating, the 15mm lens could have near perfect transmission. It is important to note that the 3 inch lens is also three times thicker than the 15mm lens, which helps explain why it is more absorptive. With proper coating, it could also have near perfect transmission.

The stack of three lenses had a higher transmission than the product of the three individual transmissions, which is unexpected. This could be due to focusing effects concentrating power on the detector, creating an artificially inflated power reading.

It is important to note that, in calculating Equation 31, an overall system efficiency of 0.85 was assumed. If a system were to be implemented using a GRIN lens stack with a diminished transmission around 0.586, then the atmospheric transmission threshold would need to increase holding all else constant. However, other variables could be changed as well such as energy per pulse, lens diameter, or beam footprint among others.

Profiling the beam through the focus revealed the 15mm lens exhibits astigmatism. The focus in the V-axis was 0.019 inches, or 0.48mm in front of the focus in the W-axis. For this reason, the beam profiles in each axis are shown at their own focuses. For comparison, first is the unfocused beam shape as it appears coming out of the collimating lens (see Fig. 28) followed by the profiles in the V- and W-axes (see Figs. 29 and 30). The collimated beam has a Gaussian correlation of 99.6% and 99.2% in the V- and W-axes, respectively. From these 1D profiles it seems that the beam is perfectly Gaussian, but looking at Fig. 28, it is clear there are imperfections in other dimensions. This is a pitfall of using only 1D profiles. Despite the limited number of profiles, the source beam can confidently be called Gaussian. The beam widths for the source beam is reported as the FWHM intensity (50%) value because the $1/e^2$ (13.5%) width was outside of the detectors upper limit of detection of 3000μm. The beam widths for the focal points are reported as the $1/e^2$ intensity point.

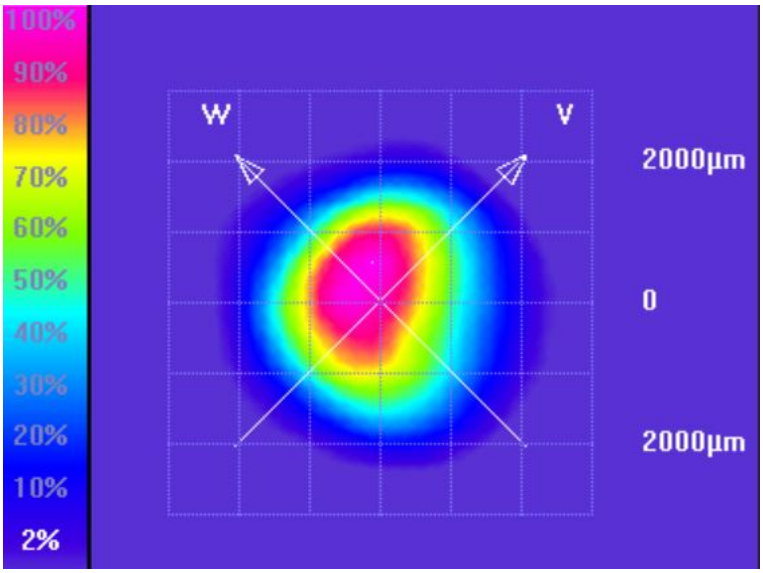

Figure 28. Collimated laser beam shape with no lens present.

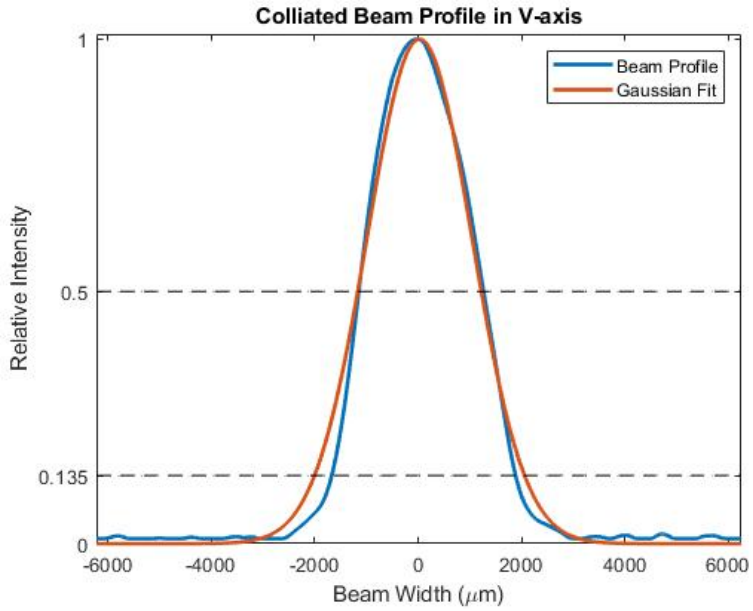

Figure 29. 1-D beam profile in V-axis and Gaussian fit of collimated laser source with no lens present. The red line is the Gaussian fit and the yellow line is the actual profile of the beam. The FWHM and $1/e^2$ levels are shown in the dashed, black lines. The FWHM beam width is 2371μm. The profile has a 99.6% Gaussian correlation.

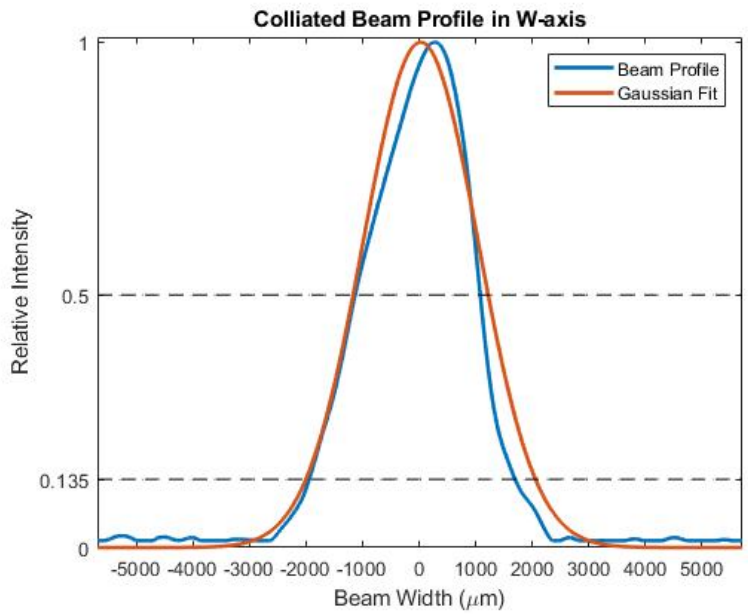

Figure 30. 1-D beam profile in W-axis and Gaussian fit of collimated laser source with no lens present. The red line is the Gaussian fit and the yellow line is the actual profile of the beam. The FWHM and $1/e^2$ levels are shown in the dashed, black lines. The FWHM beam width is 2164μm. The profile has a 99.2% Gaussian correlation.

The beam width measurement showed that the minimum width was 286.22μm at the V-axis focus and 197.29μm at the W-axis focus. The depths of focus are shown in Figs. 31 and 32. These figures track the beam width as the profiler was slid into and out of focus. The shapes of the beams when they reached their focus are shown in Figs. 33 and 34. It is clear to see that the beam shape does change between the two focal points. As such, the Gaussian fits also vary. The 1-D profiles with their fits are shown in Figs. 35 and 36. The beam is reduced to a 96% Gaussian correlation in the V-axis and a 97.6% Gaussian corrrelation in the W-axis. The lens accounts for a loss of 3.3% and 1.8% of the Gaussian shape of the beam in the V- and W-axes, respectively. This is indicative of some minor aberrations.

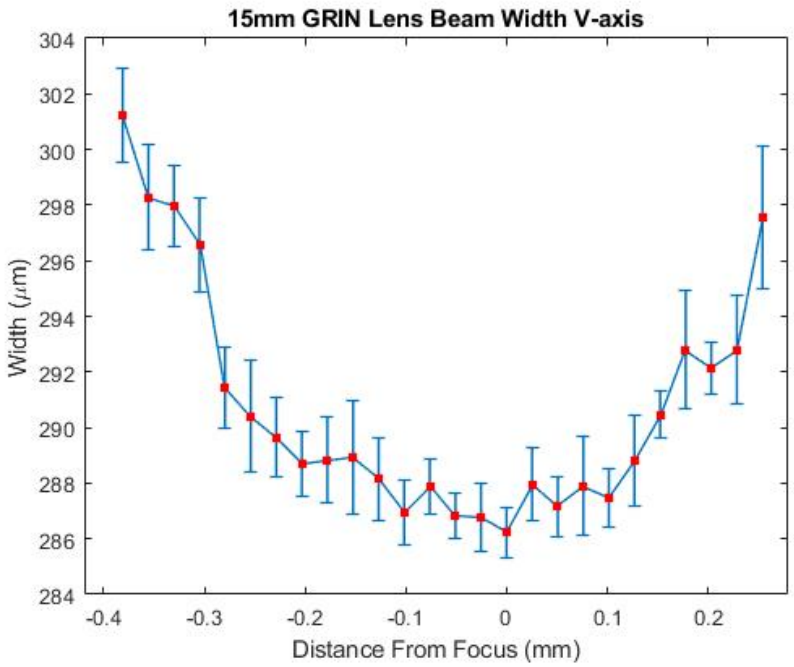

Figure 31. The beam width as it comes to and goes out of focus in the V-axis. The minimum width was 286.22μm.

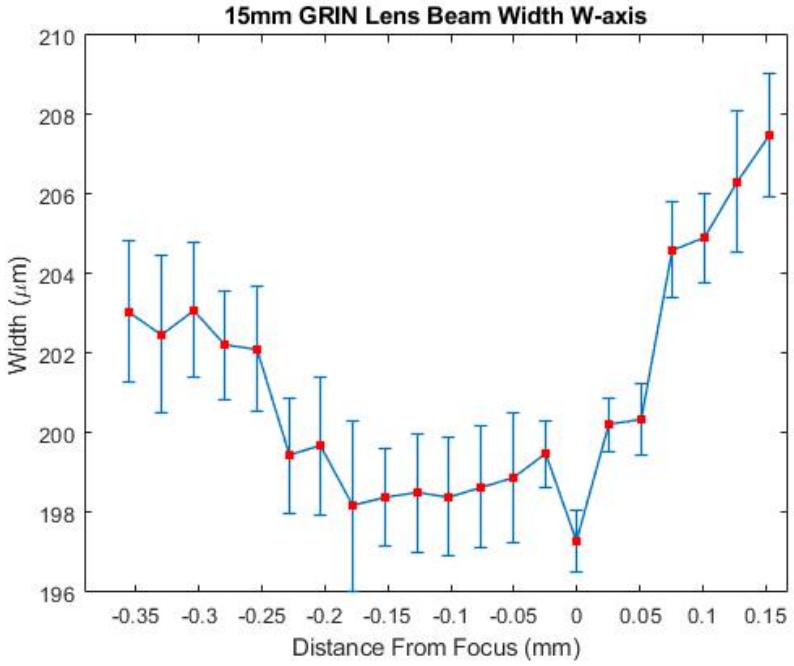

Figure 32. The beam width as it comes to and goes out of focus in the W-axis. The minimum width was 197.29μm.

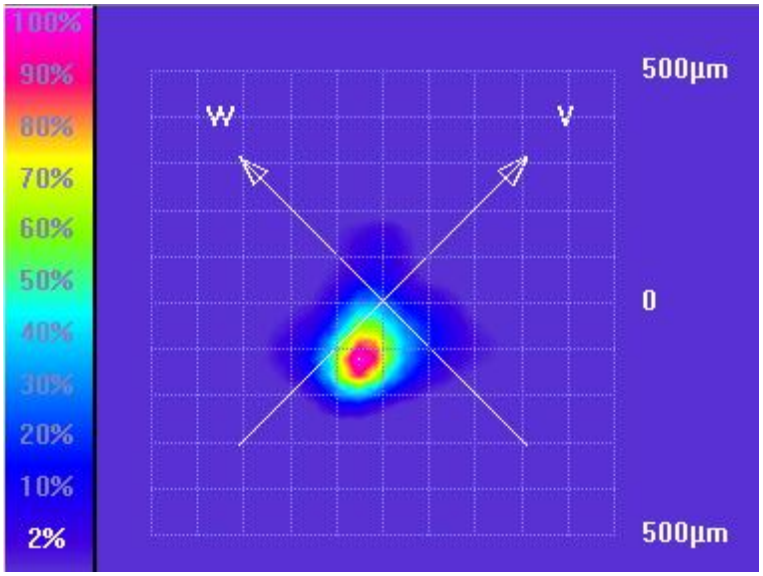

Figure 33. The beam shape at the focus in the V-axis.

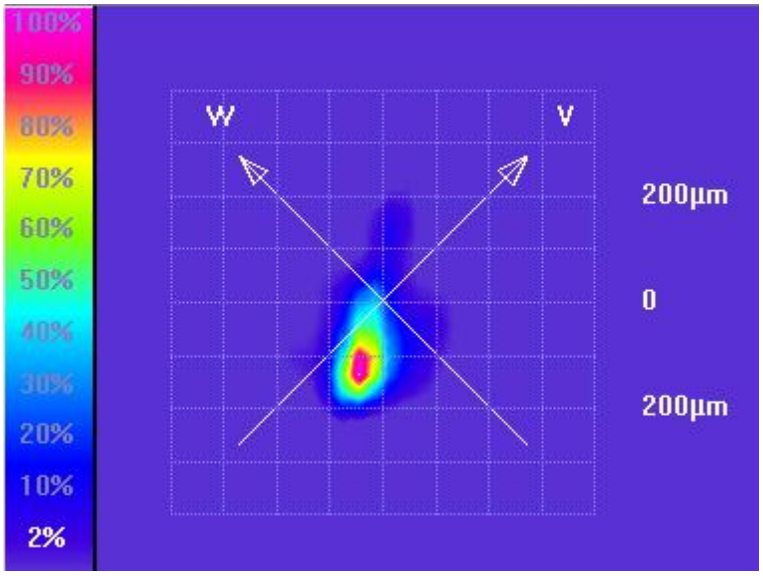

Figure 34. The beam shape at the focus in the W-axis.

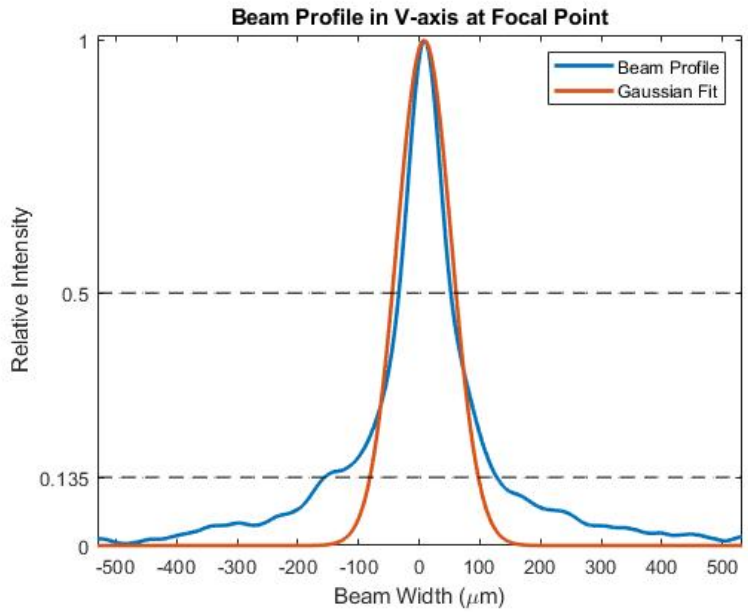

Figure 35. The 1-D beam profile when focused in the V-axis along with a Gaussian fit. The orange line is the Gaussian fit and the blue line is the actual profile of the beam. The profile has a 96% Gaussian correlation.

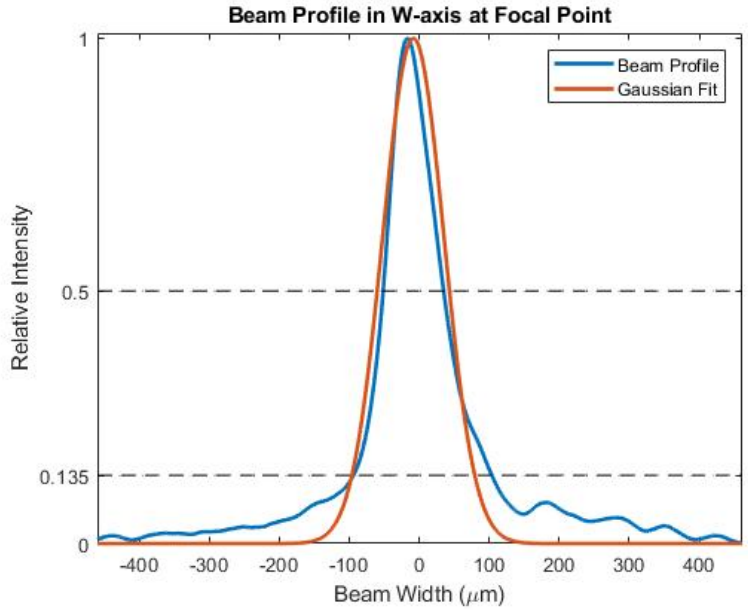

Figure 36. The 1-D beam profile when focused in the W-axis along with a Gaussian fit. The orange line is the Gaussian fit and the blue line is the actual profile of the beam. The profile has a 97.6% Gaussian correlation.

These profiles were then Fourier Transformed to find the one-dimensional MTF of the lens in each dimension, as shown in Figs. 37a and 37b. From the shape of the MTF it is clear to see that the lenses are far from diffraction limited and have poor spatial frequency resolution. These lenses are not yet technologically mature enough to be used in an imaging system

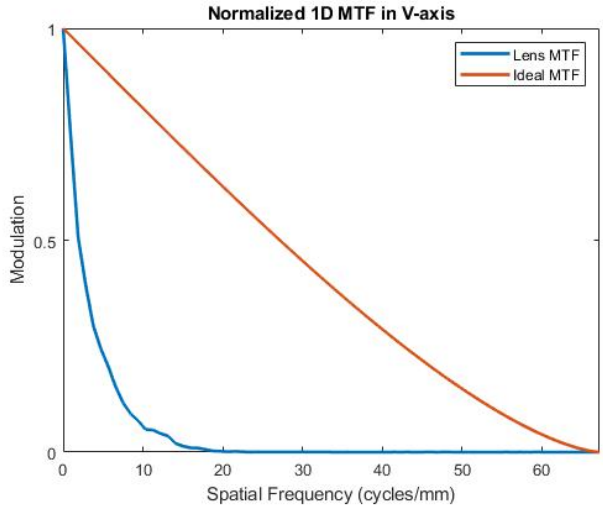

(a) MTF in the V-axis.

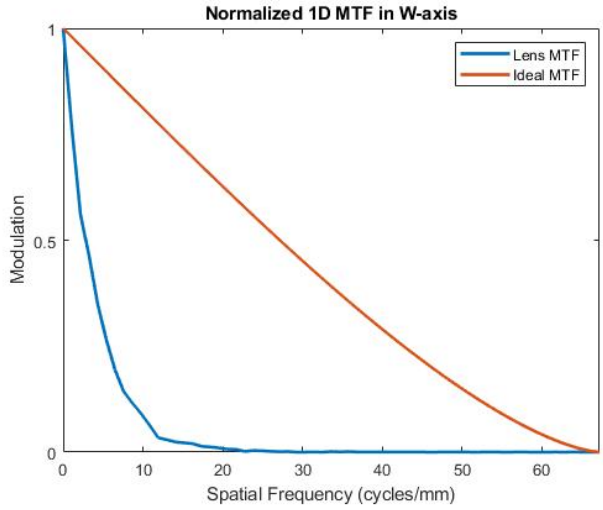

(b) MTF in the W-axis.

Figure 37. One-dimensional MTFs for the 15mm GRIN lens. Since the lens exhibited astigmatism and focused in two different points for the two axes, the MTF was computed at each focal point in its respective axis. The blue line is the MTF and the orange line represents the ideal limit which goes to zero at the cutoff frequency, 67.2 cycles/mm

This optic has good focusing power as it was able to bring the beam down to a tight focal point of only 197-286μm from an original beam width over 3000μm. However, it clearly exhibits aberrations as shown by the astigmatism and MTF. Further study is required to determine and quantify the specific aberrations this lens has.

For the case of the proposed LADAR, these optics demonstrate good throughput when considered individually. They provide advantages because they are lightweight and can be manufactured in bulk through a printing process. However, they exhibit significant aberrations and an inverse relationship with size and transmission. They require further development if they are to be scaled up in size and produce high image quality.

V. Conclusion

5.1 Contributions

This study demonstrated the validity of the LEEDR and HELEEOS models, used them to predict spaceborne LADAR system performance, and characterized GRIN optics. A collimated beacon transmissometer was assembled and tested at 543nm. The data from the transmissometer was used to partially validate HELEEOS, and thereby LEEDR, by showing an error of <5%. Given several design parameters for a hypothetical spaceborne direct detection LADAR system, a threshold atmospheric transmission necessary to maintain SNR >3 was established. LEEDR, using eleven years of historical weather data based on NWP, was used to extract PDFs of atmospheric transmission efficiency at three wavelengths − 1.06μm, 1.55μm, and 2.134μm − for three locations − Yuma, AZ, WPAFB, OH, and Point Barrow, AK.

The transmissions and focusing qualities of the GRIN lenses were determined. The GRIN lenses showed high throughput individually but transmission decreased with increasing diameter. The 15mm lens exhibited aberrations including astigmatism. It was able to maintain ≈96-97% of a ≈99% Gaussian beam.

The simulation results showed that transmission is far more influenced by location than it is by wavelength. Differences in transmission between wavelengths at the same location were no greater than 1.72% while the likelihood of exceeding the minimum threshold between locations varied by as much as 31.07%. Cloud cover was seen to be the primary factor in eliminating laser transmission, and in the case of Point Barrow, it accounted for >40% of all data points. In nearly all instances without cloud cover, the threshold efficiency is met. For a practical application, this means that when clouds are not present there will almost always be sufficient SNR with the given design parameters. Weather conditions, and not necessarily the atmospheric makeup

at various locations, are the limiting factors in maintaining a minimum atmospheric transmission at the wavelengths studied.

Moreover, it is worth noting that despite the cloud cover significantly reducing transmission and therefore SNR, it does not render this proposed LADAR moot. Passive imaging satellites have been in use for decades and similarly have imagery completely obscured by clouds. With many passes over a target area with varying weather conditions, the system would eventually build a map of the area. While not necessarily always available for real-time ISR, a spaceborne direct detection LADAR could eventually provide a 3D map of the area of interest.

It is important to note that all of these transmission values are given for a vertical path which is the best case scenario. Transmission would be lower if there was some slant path for the light to travel through. A slant path would result in a thicker atmosphere to traverse and therefore more scattering and absorption.

5.2 Future Work

Future work should encompass wider band validation of LEEDR and HELEEOS. This study only evaluated the models at a single wavelength and then used the model to evaluate three other wavelengths. The models should be valideated at the particular wavelengths of interest and beyond. Careful measurements of the beam size should be made as to provide accurate inputs to HELEEOS.

Future analyses should evaluate a greater diversity of locations within and outside of North America. Comparing multiple areas of similar climates will help form an understanding of how climate plays a roll in atmospheric transmission.

Additionally, more robust testing should be conducted on the GRIN lenses. Their specific aberrations should be identified and quantified to gain a better understanding of design constraints should they be used in a space LADAR scenario.

Bibliography

1. A. F. Chase, D. Z. Chase, C. T. Fisher, S. J. Leisz, and J. F. Weishampel, "Geospatial revolution and remote sensing lidar in mesoamerican archaeology," *Proceedings of the National Academy of Sciences*, vol. 109, pp. 12 916–12 921, 2012. [Online]. Available: https://www.pnas.org/content/109/32/12916

2. C.-K. Wang and W. D. Philpot, "Using airborne bathymetric lidar to detect bottom type variation in shallow waters," *Remote Sensing of Environment*, vol. 106, pp. 123–135, 2007. [Online]. Available: https://www.sciencedirect.com/science/article/pii/S0034425706003002

3. X. Sun, "Space-based lidar systems." Optical Society of America, 2012, p. JW3C.5. [Online]. Available: http://www.osapublishing.org/abstract.cfm?URI=QELS-2012-JW3C.5

4. E. Hecht, *Optics*, 5th ed. Pearson Education, 2017.

5. B. E. A. Saleh and M. C. Teich, *Fundamentals of Photonics*, 2nd ed. John Wiley Sons, Inc., 2007.

6. J. B. Keller, "Geometrical theory of diffraction," *Optical Society of America*, vol. 52, pp. 116–130, 2 1962.

7. W. J. Smith, *The Infrared and Electro-Optical Systems Handbook*, W. D. Rogatto, Ed. Infrared Information Analysis Center and SPIE Optical Engineering Press, 1978, vol. 3.

8. J. W. Goodman, *Introduction to Fourier Optics*, 4th ed., L. Kinne, Ed. W.H. Freeman, 5 2017.

9. J. T. Verdeyen, *Laser Electronics*, 3rd ed., N. J. Holonyak, Ed. Prentice Hall, 1995.

10. P. McManamon, *LiDAR Technologies and Systems*. Society of Photo-Optical Instrumentation Engineers, 2019.

11. B. W. Schilling, D. N. Barr, G. C. Templeton, L. J. Mizerka, and C. W. Trussell, "Multiple-return laser radar for three-dimensional imaging through obscurations," *Appl. Opt.*, vol. 41, pp. 2791–2799, 5 2002. [Online]. Available: http://ao.osa.org/abstract.cfm?URI=ao-41-15-2791

12. R. M. Marino and W. R. Davis, "Jigsaw: a foliage-penetrating 3d imaging laser radar system," *Lincoln Laboratory Journal*, vol. 15, 2005.

13. P. Cho, H. Anderson, R. Hatch, and P. Ramaswami, "Real-time 3d ladar imaging," 2006.

14. M. R. Kutteruf and P. Lebow, "1541nm gmapd ladar system," M. D. Turner, G. W. Kamerman, L. M. W. Thomas, and E. J. Spillar, Eds., 6 2014.

15. M. R. Roddewig, J. H. Churnside, F. R. Hauer, J. Williams, P. E. Bigelow, T. M. Koel, and J. A. Shaw, "Airborne lidar detection and mapping of invasive lake trout in yellowstone lake," *Applied Optics*, vol. 57, pp. 4111–4116, 5 2018.

16. E. L. Dereniak and G. D. Boreman, "Infrared detectors and systems," *Infrared Detectors and Systems*, 1996.

17. D. E. Smith, M. T. Zuber, H. V. Frey, J. B. Garvin, J. W. Head, D. O. Muhleman, G. H. Pettengill, R. J. Phillips, S. C. Solomon, H. J. Zwally, W. B. Banerdt, T. C. Duxbury, M. P. Golombek, F. G. Lemoine, G. A. Neumann, D. D. Rowlands, O. Aharonson, P. G. Ford, A. B. Ivanov, C. L. Johnson, P. J. McGovern, J. B.

Abshire, R. S. Afzal, and X. Sun, "Mars orbiter laser altimeter: Experiment summary after the first year of global mapping of mars," *Journal of Geophysical Research E: Planets*, vol. 106, 2001.

18. T. Markus, T. Neumann, A. Martino, W. Abdalati, K. Brunt, B. Csatho, S. Farrell, H. Fricker, A. Gardner, D. Harding, M. Jasinski, R. Kwok, L. Magruder, D. Lubin, S. Luthcke, J. Morison, R. Nelson, A. Neuenschwander, S. Palm, S. Popescu, C. K. Shum, B. E. Schutz, B. Smith, Y. Yang, and J. Zwally, "The ice, cloud, and land elevation satellite-2 (icesat-2): Science requirements, concept, and implementation," *Remote Sensing of Environment*, vol. 190, 2017.

19. B. E. Schutz, H. J. Zwally, C. A. Shuman, D. Hancock, and J. P. DiMarzio, "Overview of the icesat mission," *Geophysical Research Letters*, vol. 32, 2005.

20. X. Sun, J. B. Abshire, A. A. Borsa, H. A. Fricker, D. Yi, J. P. Dimarzio, F. S. Paolo, K. M. Brunt, D. J. Harding, and G. A. Neumann, "Icesat/glas altimetry measurements: Received signal dynamic range and saturation correction," *IEEE Transactions on Geoscience and Remote Sensing*, vol. 55, 2017.

21. D. Winker, W. Hunt, and C. Weimer, "The on-orbit performance of the CALIOP LIDAR on CALIPSO," in *International Conference on Space Optics — ICSO 2008*, J. Costeraste, E. Armandillo, and N. Karafolas, Eds., vol. 10566, International Society for Optics and Photonics. SPIE, 2017, pp. 378 – 385. [Online]. Available: https://doi.org/10.1117/12.2308248

22. T. A. Neumann, A. J. Martino, T. Markus, S. Bae, M. R. Bock, A. C. Brenner, K. M. Brunt, J. Cavanaugh, S. T. Fernandes, D. W. Hancock, K. Harbeck, J. Lee, N. T. Kurtz, P. J. Luers, S. B. Luthcke, L. Magruder, T. A. Pennington, L. Ramos-Izquierdo, T. Rebold, J. Skoog, and T. C. Thomas, "The ice, cloud, and land elevation satellite – 2 mission: A global geolocated photon product derived

from the aadvanced ttopographic llaser aaltimeter ssystem," *Remote Sensing of Environment*, vol. 233, 2019.

23. G. A. Neumann, D. E. Smith, and M. T. Zuber, "Two mars years of clouds detected by the mars orbiter laser altimeter," *Journal of Geophysical Research E: Planets*, vol. 108, 2003.

24. G. Thomas, R. Cobb, S. Fiorino, , and M. Hawks, "Daytime cloudless sky radiance quantification with ground-based aerosol and meteorological observations in the shortwave infrared," *Journal of Atmospheric and Oceanic Technology*, vol. 37, 2020.

25. M. T. Eismann, "Optical radiation and matter," 2012.

26. G. P. Perram, C. J. Salvatore, R. L. Hengehold, and S. T. Fiorino, *An Introduction to Laser Weapon Systems*, 1st ed. Directed Energy Professional Society, 2010.

27. S. T. Fiorino, R. M. Randall, M. F. Via, and J. L. Burley, "Validation of a uv-to-rf high-spectral-resolution atmospheric boundary layer characterization tool," *Journal of Applied Meteorology and Climatology*, vol. 53, 2014.

28. J. E. Schmidt, J. L. Burley, B. J. Elmore, S. T. Fiorino, K. J. Keefer, and N. R. V. Zandt, "Defense innovation handbook guidelines, strategies, and techniques," pp. 257–279, 2018.

29. S. T. Fiorino, S. R. Bose-Pillai, J. E. Schmidt, B. J. Elmore, and K. J. Keefer, "Implications of four-dimensional weather cubes for improved cloud-free line-of-sight assessments of free-space optical communications link performance," *Optical Engineering*, vol. 59, 7 2020.

30. N. R. V. Zandt, S. T. Fiorino, and K. J. Keefer, "Enhanced, fast-running scaling law model of thermal blooming and turbulence effects on high energy laser propagation," *Optics Express*, vol. 21, 2013.

31. S. T. Fiorino, R. J. Bartell, M. J. Krizo, G. Caylor, K. P. Moore, T. Harris, and S. J. Cusumano, "Worldwide uncertainty assessments of ladar and radar signal-to-noise ratio performance for diverse low altitude atmospheric environments," *Journal of Applied Remote Sensing*, vol. 4, p. 1 – 19, 2010. [Online]. Available: https://doi.org/10.1117/1.3457165

32. E. W. Marchand, *Gradient index optics*. Academic Press, 1978.

33. P. Gatt and S. W. Henderson, "Laser radar detection statistics: a comparison of coherent and direct-detection receivers," G. W. Kamerman, Ed., 9 2001.

34. M. A. Itzler, U. Krishnamachari, M. Entwistle, X. Jiang, M. Owens, and K. Slomkowski, "Dark count statistics in geiger-mode avalanche photodiode cameras for 3-d imaging ladar," *IEEE Journal of Selected Topics in Quantum Electronics*, vol. 20, 11 2014.

35. C. Wu, J. R. Rzasa, J. Ko, D. A. Paulson, J. Coffaro, J. Spychalsky, R. F. Crabbs, and C. C. Davis, "Multi-aperture laser transmissometer system for long-path aerosol extinction rate measurement," *Appl. Opt.*, vol. 57, no. 3, pp. 551–559, Jan 2018. [Online]. Available: http://ao.osa.org/abstract.cfm?URI=ao-57-3-551

36. Newport, *Knife-Edge Profiler Manual*, Newport.

37. *818 Series Photodetector Guide*, Newport Corporation.

38. *MAGIC Water Condensation Particle Counter*, Aerosol Devices Inc.

39. J. R. Taylor, *An Introduction to Error Analysis*, 2nd ed., A. McGuire, Ed. University Science Books, 1997.

40. S. T. Fiorino, R. J. Bartell, M. J. Krizo, G. L. Caylor, K. P. Moore, T. R. Harris, and S. J. Cusumano, "A first principles atmospheric propagation amp; characterization tool: the laser environmental effects definition and reference (leedr)," O. Korotkova, Ed., 2 2008.

REPORT DOCUMENTATION PAGE

Form Approved
OMB No. 0704–0188

1. REPORT DATE *(DD–MM–YYYY)*	2. REPORT TYPE	3. DATES COVERED *(From — To)*
21-06-2021	Master's Thesis	Aug 2020 — Jun 2021

4. TITLE AND SUBTITLE

Analysis of Space-to-Ground LADAR Performance with Non-Traditional Optics

5a. CONTRACT NUMBER

5b. GRANT NUMBER

5c. PROGRAM ELEMENT NUMBER

6. AUTHOR(S)

Hanjra, Prayant P.S., 1st Lt

5d. PROJECT NUMBER

5e. TASK NUMBER

5f. WORK UNIT NUMBER

7. PERFORMING ORGANIZATION NAME(S) AND ADDRESS(ES)

Air Force Institute of Technology
Graduate School of Engineering and Management (AFIT/EN)
2950 Hobson Way
WPAFB OH 45433-7765

8. PERFORMING ORGANIZATION REPORT NUMBER

AFIT-ENP-MS-21-S-030

9. SPONSORING / MONITORING AGENCY NAME(S) AND ADDRESS(ES)

David Rabb
AFRL/RYMM
3109 Hobson Way, WPAFB, OH 45433

10. SPONSOR/MONITOR'S ACRONYM(S)

11. SPONSOR/MONITOR'S REPORT NUMBER(S)

12. DISTRIBUTION / AVAILABILITY STATEMENT

Distribution Statement A:
Approved for Public Release; Distribution unlimited.

13. SUPPLEMENTARY NOTES

14. ABSTRACT

Two major obstacles to space-based LADAR systems are low power returns from targets and limitations on size and weight for transporting large optics into orbit. Signals incur significant losses during roundtrip propagation through the atmosphere and from diffuse scattering off of targets. Models, such as the Laser Environmental Effects Definition and Reference (LEEDR) simulator and High Energy Laser End to End Operational Simulation(HELEEOS) can predict these losses due to the atmosphere and optical components for a variety of atmospheric and environmental conditions across the globe. A transmissometer is used to validate these models. These losses are used to determine if sufficient power would reach a space-borne receiver. One way of ensuring sufficient power is to increase the size of the optic. For this reason, optics in space tend to be large. However, to get desired performance, these optics quickly become prohibitively large and heavy to transport in a satellite. Many non-traditional optics have emerged in recent years that show promise for providing lightweight and volume constrained solutions polymer-based, gradient index (GRIN) optics. These optics were acquired and characterized for their potential use in creating large direct detection LADAR system in space. The results from these characterizations were used to provide feedback on photon link budgets. The feasibility of space based direct detection LADAR is reported from a radiometric standpoint.

15. SUBJECT TERMS

Light detection and ranging, direct detection, non-traditional optics, space sensing, gradient index, atmospheric losses, LEEDR, HELEEOS

16. SECURITY CLASSIFICATION OF:			17. LIMITATION OF ABSTRACT	18. NUMBER OF PAGES	19a. NAME OF RESPONSIBLE PERSON
a. REPORT	b. ABSTRACT	c. THIS PAGE			Dr. Steven Fiorino, AFIT/ENP
U	U	U	UU	86	19b. TELEPHONE NUMBER *(include area code)* (937)255-3636 x4506